



OPEN Erratic behavior of platinum-group elements along an olivine–Cr-spinel cotectic in sulfide-undersaturated basaltic magma: roles of Cr-spinel and alloys

Ivan. F. Chayka¹, Vadim S. Kamenetsky^{2,3✉}, Anton V. Kutyrev^{4,14}, Sarah-Jane Barnes⁵, Aleksandr S. Stepanov⁶, Sergey E. Konstantinov^{7,8}, Nikolay I. Baykov¹, Sergey G. Kryazhev⁹, Ivan A. Belousov¹⁰, Irina A. Zhukova⁶, Vasily D. Scherbakov¹¹, Valery M. Kalugin⁹, Alexey V. Ivanov¹², Nikolay V. Bryanskiy¹² & Jung-Woo Park¹³

The behavior of platinum-group elements (PGE) in sulfide-undersaturated primitive magmas may be controlled by crystallization of either Cr-spinel, platinum-group minerals (PGM) or olivine. Evaluation of the PGM-hosted PGE portion is challenging because PGM in volcanic rocks are small and rare. We report on the sizes and compositions of PGM associated with Cr-spinel, the PGE content of Cr-spinel and olivine, and the bulk rock PGE content from sulfide undersaturated arc volcanics of the Tumrok range (Eastern Kamchatka). Platinum-iron and Ir-Os alloys (< 30 to > 3000 nm in size) form inclusions in Cr-spinel. Their presence and composition are mostly independent of Cr-spinel chemistry. Bulk rock PGE contents are erratic and PGE concentrations in Cr-spinel are exceptionally variable (up to 2 orders of magnitude). Whereas PGM inclusions in Cr-spinel and PGE in solid solution in Cr-spinel significantly contribute to the bulk rock PGE budget, a considerable portion of the PGE must be present associated with minerals other than Cr-spinel. The variable PGE content of the rocks is attributed to a combination of: (a) disequilibrium kinetic effects at the Cr-spinel–melt boundary layer, strongly affecting PGE partitioning into Cr-spinel and crystallization of PGM in the layer; (b) the presence of some sufficiently large PGM to cause nugget effects; and (c) melt degassing.

Platinum-group elements (PGE) have a strong affinity for sulfide melts, and PGE deposits are largely hosted by sulfide-bearing mafic and ultramafic rocks^{1,2}. Primitive magmas typically reach the crust undersaturated in sulfide liquid, and extensive fractional crystallization and crustal assimilation are necessary to promote sulfide liquid saturation^{1–3}. The behavior of PGE prior to sulfide saturation and the factors controlling their partitioning remain debated. Some studies of chromite-rich plutonic rocks propose that the platinum-group minerals

¹Korzhinskii Institute of Experimental Mineralogy RAS, Chernogolovka 142432, Russia. ²Center of Deep Sea Research, Institute of Oceanology, Chinese Academy of Sciences, Qingdao 266071, P. R. China. ³Institute of Volcanology and Seismology FEB RAS, Piipa 9, Petropavlovsk-Kamchatsky 683006, Russia. ⁴School of Geosciences, University of the Witwatersrand, 1 Jan Smuts Avenue, Johannesburg 2050, South Africa. ⁵Sciences de la Terre, Université du Québec à Chicoutimi, Québec G7H 2B1, Canada. ⁶State Key Laboratory of Geological Processes and Mineral Resources, Collaborative Innovation Center for Exploration of Strategic Mineral Resources, School of Earth Resources, China University of Geosciences (Wuhan), Wuhan 430074, China. ⁷Budker Institute of Nuclear Physics SB RAS, Novosibirsk 630090, Russia. ⁸Novosibirsk State University, Novosibirsk 630090, Russia. ⁹Central Research Institute of Geological Prospecting for Base and Precious Metals (TsNIGRI), 1-129 Warshawskoe Chaussee, Moscow 117545, Russia. ¹⁰CODES, University of Tasmania, Hobart, Australia. ¹¹Department of Petrology and Volcanology, Faculty of Geology, Moscow State University, Leninskie Gori, 1, Moscow 119991, Russia. ¹²Institute of the Earth's Crust, Siberian Branch of the Russian Academy of Science, Irkutsk 664033, Russia. ¹³School of Earth and Environmental Sciences, Seoul National University, Seoul 08826, South Korea. ¹⁴African Research Centre for Ore System Science (CORES), School of Geosciences, University of the Witwatersrand, 1 Jan Smuts Avenue, Johannesburg, South Africa. ✉email: Dima.Kamenetsky@hotmail.com

crystallize alongside of Cr-spinel^{4–6}, while others suggest that PGE are mainly concentrated by Cr-spinel and exsolve from the host to form PGM upon cooling^{7,8}.

Studying the behavior of PGE and the magmatic crystallization of PGM is complicated by at least two factors. First, PGE concentrations in most magmatic rocks are extremely low (ppb to ppt), and PGM are very small and unevenly dispersed throughout the rock matrix. This significantly restricts quantitative assessments of the PGE behavior based on empirical data. Second, plutonic rocks, in which PGE form ore concentrations and upon which most studies of PGE geochemistry have been based^{4–9}, undergo post-crystallization modifications that distort the primary magmatic distribution of the PGE. These include but are not limited to: exsolution of PGE from the Cr-spinel lattice to form post-solidus PGM, decomposition of sulfides and fluid-driven transport of PGE.

Examination of the behavior of PGE in volcanic rocks offers the opportunity to avoid these post-crystallization effects. Empirical data from primitive sulfide-undersaturated volcanic rocks show that their PGE concentrations may either follow well-defined fractionation trends or appear scattered, even within a single magmatic series^{10–16}. In the absence of sulfide saturation, Cr-spinel has been shown to concentrate IPGE (Os, Ir, Ru) and Rh (contents up to 350 ppb, with $D_{\text{PGE}}^{\text{Chr/melt}}$ up to 3700) presumably as a solid solution in the crystal lattice (hereinafter referred to as “admixture”)^{17–23} and thus potentially controls the budget of these elements. On the other hand, Pagé and Barnes (2016) and Barnes (2024)^{17,20} demonstrated that contents of IPGE and Rh in Cr-spinel are insufficient to account for the entire budget of IPGE and Rh in mafic and ultramafic volcanic rocks. Direct crystallization of PGE-bearing minerals and alloys (PGM) in primitive magmas is supported by rare observations of micrometre-sized PGM inclusions in magmatic Cr-spinel from volcanic rocks^{10,22,24–26} and is inferred from the broad dispersion of bulk Pt contents (nugget effect) and its compatible behavior in some sulfide-undersaturated basalts^{14,15}. These implications are in line with experimental studies which conclude that “nugget fractionation simply is more likely than PGE substitution in the crystal lattice of chromite”²⁷ and “nanonuggets can be a means to transport PGE at much higher concentrations than can be dissolved in silicate magmas”²⁸. Thus, substantial evidence for both Cr-spinel and PGM controlling behavior of PGE in sulfide-undersaturated basaltic magma requires a more detailed assessment of these processes during early stages of crystallization of such a magma.

In our study, the behavior of PGE is addressed in primitive, highly-oxidized, sulfide-undersaturated arc picrites and basalts of the Tumrok range, eastern Kamchatka^{29–31}. In addition to bulk rock, Cr-spinel and silicate mineral PGE analyses, a statistical examination of PGM inclusions in Cr-spinel, including (1) their compositional relationships along the olivine – Cr-spinel cotectic, and (2) an attempt to estimate their proportion in the magma PGE budget has been carried out. The study has two outcomes. First, we highlight and numerically assess the importance of PGM crystallization and variations of PGE contents in Cr-spinel, which both depend on local kinetic factors and make PGE behavior complex and erratic. Second, we develop a semi-quantitative approach utilizing laser ablation inductively-coupled plasma spectroscopy (LA ICP MS) and automated secondary electron microscopy (SEM) to find micro- to nanoscale PGM inclusions and assess mass ratios of these inclusions to the host Cr-spinel and, hence, their proportion in the bulk rock PGE budget.

Geological background

The Tumrok volcano-plutonic complex is located in eastern Kamchatka (Russia) within the Late Cretaceous – Paleogene Achaivayam-Valaginsky (also known as Olyutorsky) island-arc terrane^{31,32} (Fig. 1A, B). The mafic-ultramafic volcanics and subvolcanics are inferred to be co-genetic with plutonic rocks, which comprise dunites, wehrlites, and gabbros, forming the Ural-Alaskan type assemblage^{29,33} (Fig. 1B). The volcanics and subvolcanics form pillow lavas, tuffs, sills, and dykes (Fig. 1C, D) which are composed of olivine-phyric rocks (picrites) (Fig. 1E, F; Fig. S1A, B), and clinopyroxene-bearing basalts (Fig. S1C). Picrites are composed of large (up to 2.5 cm) partially serpentinized olivine phenocrysts, which contain Cr-spinel inclusions and a groundmass composed of clinopyroxene and magnetite, set within a matrix of serpentinite and chlorite. Sub-phenocrysts (up to 1 mm) of Cr-spinel and clinopyroxene (up to 5 mm) occur sporadically in picrites (Fig. S1A, B). Based on their chemical composition^{29,30}, all olivine and Cr-spinel are products of liquidus crystallization, not xenocrysts. Basalts are composed by clinopyroxene phenocrysts (up to 1 cm), occasional serpentinized olivine phenocrysts and groundmass formed by clinopyroxene, plagioclase, chlorite and magnetite (Fig. S1C). Chromian spinel as inclusions in clinopyroxene is very rare in basalts. Picrites and basalts are considered to have formed from a single parental melt via accumulation and fractionation of olivine (78–94 mol% Fo), Cr-spinel (38–72 mol% Mg#, 70–90 mol% Cr#, 0.85–2.5 Fe²⁺/Fe³⁺) and clinopyroxene (71–90 mol% Mg#)^{29,30}. The picrites are assumed to represent a mixture of near-primitive melt and cumulus olivine and Cr-spinel. The basalts are assumed to be a mixture of variably differentiated melt and < 15 vol% clinopyroxene phenocrysts. The Tumrok magmas, enriched in common subduction-related components (e.g., K, Sr, Ba), were derived by extensive melting (0.74–0.96 La_N/Sm_N) of a strongly depleted mantle wedge (εNd = + 10.5; εHf = + 20)^{13,29,30,34}. Based on the highest MgO content in Cr-spinel-hosted melt inclusions²⁹ and MgO–Cr regression (Fig. 2A), MgO and Cr contents in the parental melt were estimated as ~ 15 wt% and 950 ppm, respectively.

For the current work, PGE were determined (Table S1) in 5 picrites and 6 basalts, which bulk rock major and trace element analyses were reported in Chayka et al. (2023)²⁹. The PGE content in Cr-spinel and the size and composition of Cr-spinel hosted PGM inclusions were studied mainly in the 21AK9c picrite sample which contains the highest MgO (34.9 wt%) and Cr (2829 ppm) content indicative of abundant olivine and Cr-spinel phenocrysts. Both olivine and Cr-spinel show broad compositional ranges (Table S2, S3; Fig. S2), and we assume that this sample represents a mixture of transporting magma and olivine phenocrysts with Cr-spinel inclusions, and Cr-spinel sub-phenocrysts from a magmatic chamber and, thus, can be considered as a record of the olivine–Cr-spinel cotectic of the Tumrok volcanic complex in general. In addition, to confirm observations

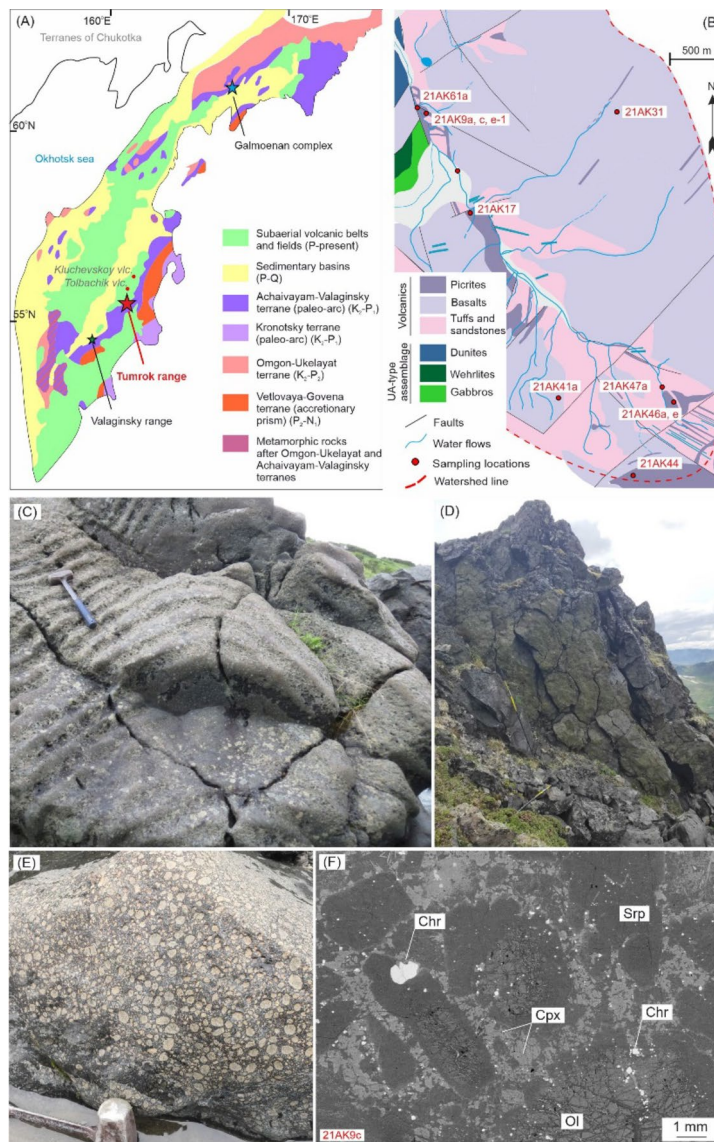


Fig. 1. Geological background and petrography of the Tumrok volcanics. **(A)** Geological map of Kamchatka peninsula (after⁶³); **(B)** geological map of the Tumrok complex (after an unpublished sketch of Markovsky B.A. and Chayka et al.²⁹) with locations of the samples studied; **(C)** an outcrop of a picrite sill; **(D)** an outcrop of basaltic pillow-lavas; **(E)** a close-up photo of picrite in a boulder: olivine phenocrysts are beige, groundmass is dark; **(F)** a SEM BSE photo of a thin section of the 21AK9c picrite: Ol – olivine, Chr – Cr-spinel, Cpx – clinopyroxene, Srp – serpentine.

from 21AK9c, PGM inclusions data and some laser ablation inductively-coupled plasma mass-spectrometry (LA ICP-MS) analyses were acquired on picrite sample 21AK17 (28.9 wt% MgO and 1968 ppm Cr) (Table S2).

Results and discussion

PGE in rocks and minerals

Bulk rock Ru, Rh, Ir, and Pt of the suite positively correlate with MgO and Cr (Fig. 2B, C, D; Fig. S3A) and are typically higher in picrites than in basalts (Fig. 3). The observed trends define concentrations of Rh, Ir, and Pt in the parental melt (950 ppm Cr) as 0.75, 0.2 and 9.5 ppb, respectively (Fig. 2B, C, D). Palladium behaves incompatibly (Fig. S3B), suggesting that sulfide saturation did not occur. Osmium shows no systematic trends in picrites, yet it is depleted in basalts, mostly below the detection limit (0.07 ppb) (Fig S3C). Nevertheless, some basalts show elevated concentrations of Ir, Os, Ru, and Pt – in many cases as high as in picrites – and, in general, PGE show a broad scattering in basalts (Fig. 2C, D and Fig. 3; Fig. S3).

Cr-spinel from the picrites is characterized by variable Mg# and Cr# (30–75 mol% and 65–90 mol%, respectively) (Fig. S2). The range of Mg# of Cr-spinel corresponds to 82–94 mol% Fo of liquidus olivine, which represents the range of the olivine – Cr-spinel cotectic in the Tumrok magmas³⁰, and in this study, we assume that Cr-spinel alteration and re-equilibration at cooling were negligible. After exclusion of PGE spikes from the

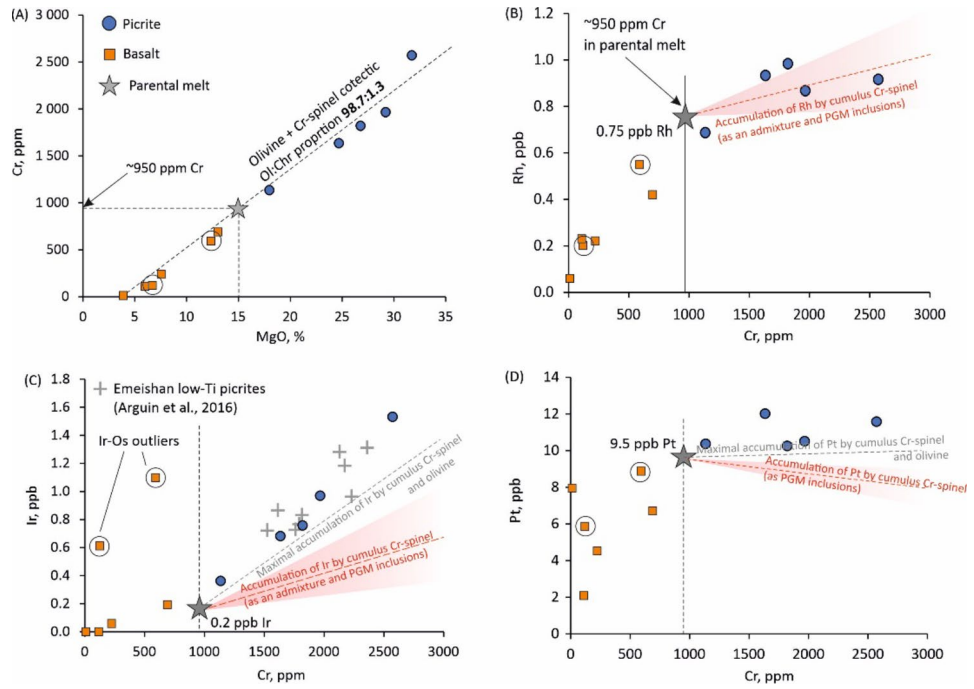


Fig. 2. Chemical variation plots with bulk rock compositions of the Tumrok complex. (A) – Cr vs. MgO plot with denoted MgO and Cr contents in a suggested parental melt; (B) Rh vs. Cr plot; (C) Ir vs. Cr plot with compositions of the low-Ti Emeishan picrites¹⁰ plotted for comparison; (D) Pt vs. Cr plot. At (B–D) panels reconstructed contents of PGE in the parental melt are plotted and calculated Cr-spinel + olivine accumulation trends with the error ranges are given. Red dashed lines denote calculated Cr-PGE trends during olivine + Cr-spinel accumulation assuming that olivine is PGE-free, pink fields are ranges of uncertainty for these trends (see main text and Methods for details), grey dashed lines denote calculated Cr-PGE trends during olivine + Cr-spinel accumulation assuming PGE contents in Cr-spinel to be the highest and PGE contents in olivine equal to their detection limits (highest possible, as well).

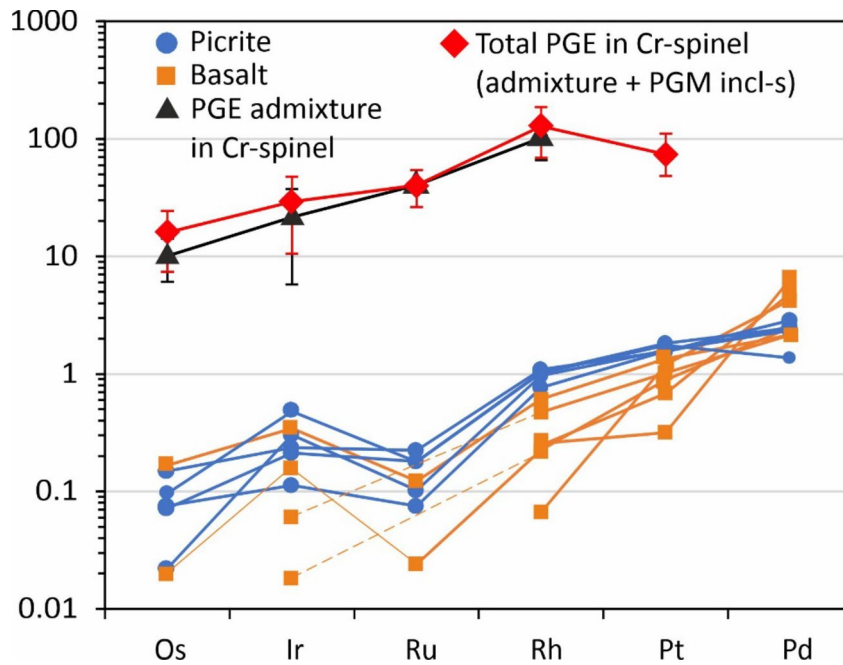


Fig. 3. A primitive-mantle (PM-) normalized spider-diagram with the plotted composition of the studied picrites and basalts, average PGE contents in Cr-spinel excluding (PGE admixture only) and including Cr-spinel-hosted PGM inclusions. PM values for normalization are from⁶⁴.

time-resolved spectra, LA ICP MS analyses ($N=128$) on grains extracted by gravitational separation and hand-picking from 21AK9c picrite show that Cr-spinel contains broad ranges of Rh: 33–183 (median 93) ppb; Ru: 110–300 (median 216) ppb; Ir: 1–172 (median 66) ppb; and Os: 11–70 (median 36) ppb admixtures (Fig. 4; Figs. S4, S5 Table S2). Additional LA ICP MS analyses on Cr-spinel from 21AK17 picrite ($N=22$) fall into the same ranges, but were not used in statistical processing and calculation because of larger error ranges (Supplementary Information). The time resolved analyses (TRA) for Pt show peaks presumably due to the presence of small Pt-Fe inclusions (see next sub-chapter). Aside from these peaks, the concentrations of Pt are largely below the detection limit (2 ppb).

Correlation analysis executed using Spearman rank correlation coefficients (as for nonparametric distributions) with a Student's test of significance level (p) shows that the PGE contents of chromite are either uncorrelated or very weakly correlated with the Cr-spinel compositions (Mg#, Cr#, $(\text{Fe}^{3+}/\text{Fe}^{2+})$, $\text{Fe}^{3+}/(\text{Cr} + \text{Al} + \text{Fe}^{3+})$, Al_2O_3 , and TiO_2). The correlations among the PGE in Cr-spinel are very poor as well (Fig. 4A, B, C; Figs. S4, S5). The most significant ($p < 0.001$) are correlations in pairs Rh–Cr₂O₃, Rh–TiO₂, Rh– $\text{Fe}^{3+}/(\text{Fe}^{3+} + \text{Cr} + \text{Al})$, Os–Rh, and Os–Ru. Iridium shows the broadest scattering and does not have apparent correlations with any other elements in Cr-spinel, yet statistical tests show that it may be positively and negatively correlated with Ru and Rh, respectively (Fig. 4B, C; Figs. S4, S5). The compositions obtained are largely in line with PGE– Fe^{3+} (Fig. 4A–C) and K_d – $f(\text{O}_2)$ (Fig. 4D) systematics of volcanic Cr-spinel worldwide²², supporting that an increase of $f(\text{O}_2)$ increases IPGE and Rh compatibility in Cr-spinel^{18,22,23} but the scattering of the PGE values even within the single sample, is exceptional and overlaps with Cr-spinel composition of various occurrences. (Fig. 4B, C).

The concentrations of PGE in olivine, clinopyroxene, and groundmass serpentine are largely below the detection limits, which are 1 ppb for Ir, 3–4 ppb for Pt, 4–5 ppb for Os, 5 ppb for Ru, and 9 ppb for Rh. Less than a half of olivine analyses show detectable Ru in a range of 5–12 ppb, but it is not clear whether they result from isobaric argide interferences from Ni and Co (Table S3).

PGM inclusions in Cr-spinel

A nanometer Pt-Fe inclusion has been found in situ in a Cr-spinel crystal, itself enclosed within an olivine phenocryst (Fig. 5A, B), confirming that Pt-Fe alloys can crystallize from melt along an olivine – Cr-spinel cotectic. Nevertheless, due to an extreme scarcity of such inclusions, the main electron microscopy data on PGM in Cr-spinel were acquired by both automated and manual search on exposed surfaces of $\sim 10^5$ grains in Cr-spinel concentrates with the total exposed area of Cr-spinel $\sim 300 \text{ mm}^2$ (see Methods and Table S4 for the details). In total, there were found 26 PGM inclusions in 21AK9c Cr-spinel and 10–21AK17 in Cr-spinel (Fig. 5C, D; Fig. S6A–U; Table S4). The exposed cuts of the inclusions are mostly isometric, resembling sections of a cube with rounded edges and vary in size from 300 nm to 1 μm (23 inclusions), occasionally reaching up to 3.3 μm (5 inclusions) (Fig. 6A; Fig. S6A–U; Table S4). The PGM are dominated by Pt-Fe alloys with a stoichiometry close

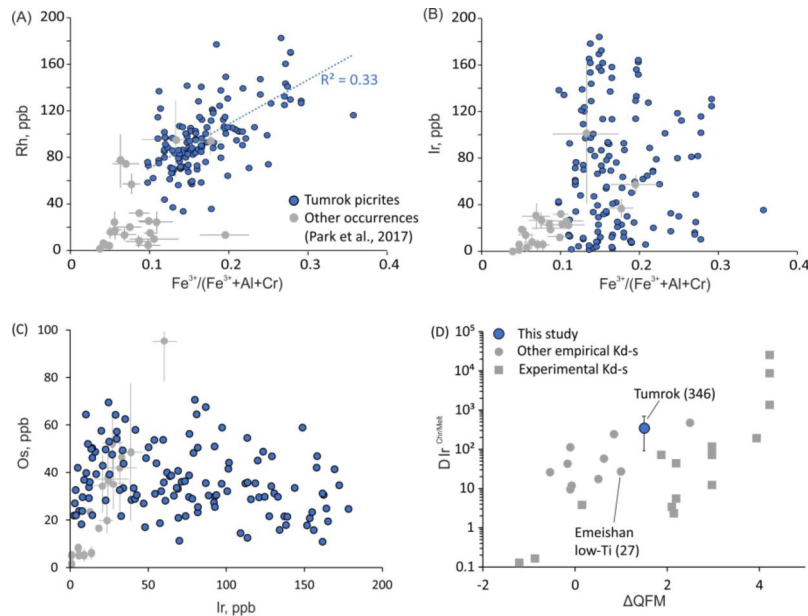


Fig. 4. Chemical variation plots with concentrations of PGE in Cr-spinel from 21AK9c (A–C) and inferred $K_d^{\text{Chr-melt}}$ (Ir) plotted versus $f(\text{O}_2)$ for the Tumrok picrites compared to other empirical and experimental data (D). Error bars for the points denoting element variations in Cr-spinel from volcanic occurrences worldwide correspond to 1 SD in analysis arrays from Park et al.²³. Error bars for the $K_d^{\text{Chr-melt}}$ (Ir) for the Tumrok complex Cr-spinel correspond to 1 SD of the array of individual $C_{\text{Chr}}(\text{Ir})/C_{\text{Chr-melt}}(\text{Ir})$ obtained in this study. $f(\text{O}_2)$ for the Tumrok picrites is after Kamenetsky et al.³⁰. Empirical $K_d^{\text{Chr-melt}}$ (Ir) are from Park et al.²³ and references therein and Pagé and Barnes²⁰ and references therein. Experimental $K_d^{\text{Chr-melt}}$ (Ir) are from Brenan et al. and Righter et al.^{18,65}.

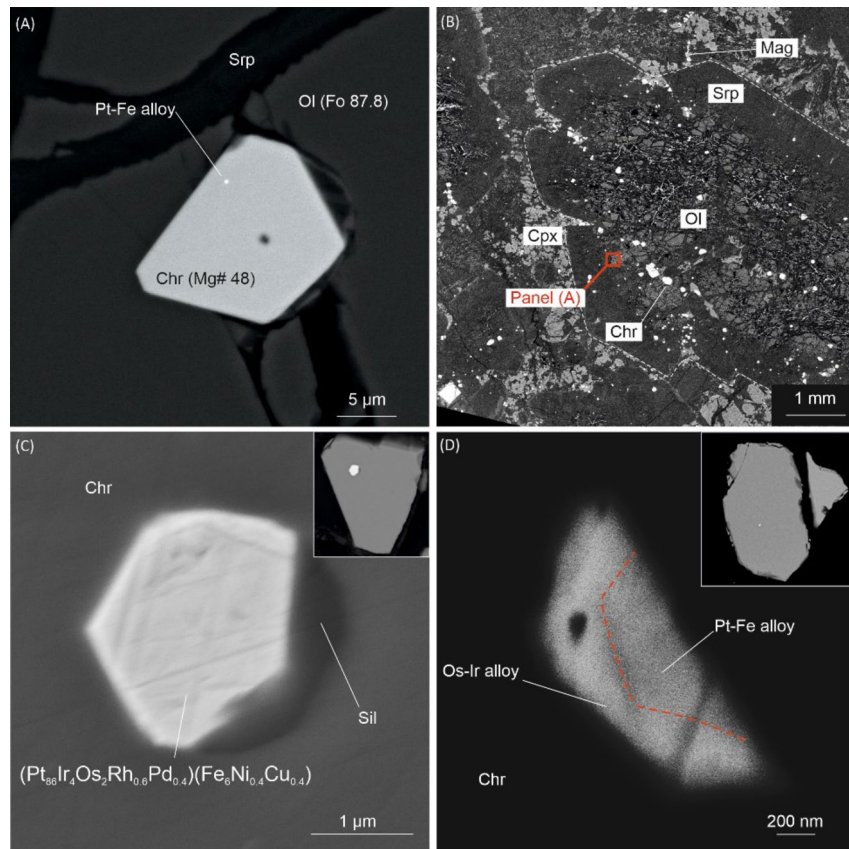


Fig. 5. PGM inclusions in Cr-spinel from the Tumrok picrites (BSE-photomicrographs). (A,B) a Pt-Fe alloy in a Cr-spinel grain (A), which is included into olivine phenocryst (outlined at panel B). (C) the second largest Pt-Fe alloy inclusion in Cr-spinel with a silicate attachment, representing former melt (picrite 21AK9c); the formula given is according to EDS analysis recalculated on Cr-spinel-free basis; (D) a composite PGM inclusion, composed by Pt-Fe and Ir-Os alloys (outlined by red dashed line). On the small insets at (C,D) are Cr-spinel grains containing these inclusions.

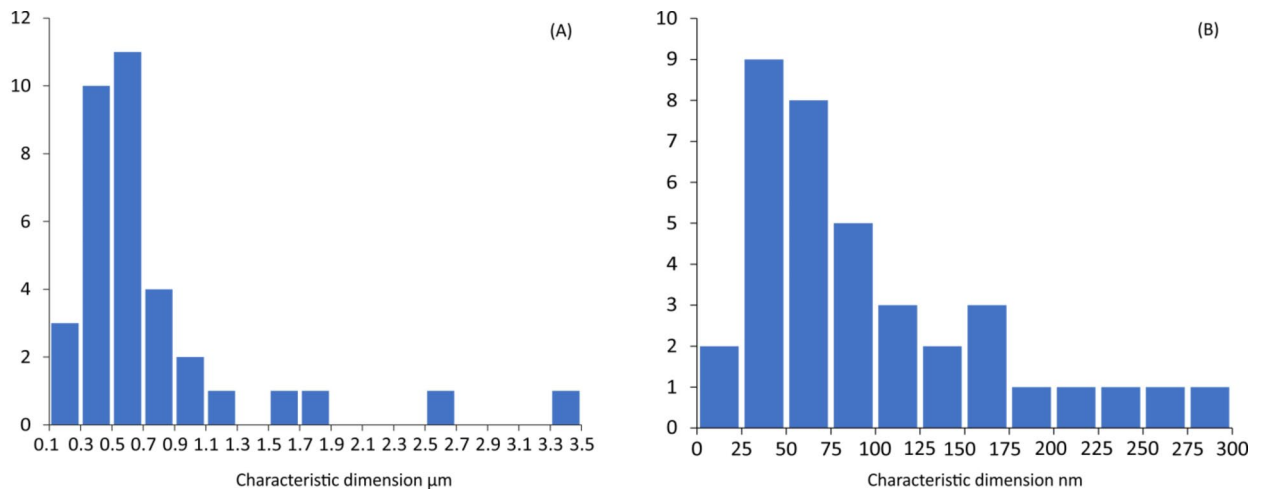


Fig. 6. Histograms illustrating size distribution of the PGM inclusions in Cr-spinel. (A) according to SEM EDS data, (B) according to LA ICP-MS data. Size is given as a “characteristic dimension”, which is a cubic root from volume estimated by LA ICP-MS and square root from area calculated from SEM images.

to isoferroplatinum and containing Cu (<2.1%), Ni (<0.6%), Ir (<8%), Os (<2%), Rh (<1.5%) and, occasionally, Pd (<0.7%) (Table S5). Many inclusions in Cr-spinel contain both alloys and silicates, forming together negative crystal shapes within the host Cr-spinel (Fig. 5C; Fig. S6B, C,G, K,L, O,Q). The silicates contain Si, Mg, Fe, Ca, K, and Al, and likely represent silicate melt entrapped along with the PGM but are too small for quantitative analysis. Additionally, two occurrences of Os-Ir alloys intergrown with Pt-Fe have been identified by SEM (Fig. 5D; Fig. S6K).

Time-resolved LA-ICP-MS spectra demonstrate numerous Pt-Fe alloy inclusions, revealed as Pt spikes (to avoid occasional “background” spikes we took into account those spikes which occupy 3 sweeps and more if only one PGE is present, while single- sweeps spikes were considered only if there are several PGE in the spike) (Fig. 7; Figs. S7A-O, S8; Tables S6, S7). In many cases, these spikes coincide with weaker signals of Ir, Os and, in some cases, Ru and Rh (Fig. 7A). Inclusions which consist mainly of Os or Ir without or with minor Pt are less common (Fig. 7B). A few inclusions containing Pd, Cu, Ni and Ru were found as well (Fig. S7G, J; Tables S6, S7). A rough quantification of the LA ICP-MS data (see Methods) shows that the PGM particles found by this method vary in size from 30 to 300 nm and their abundance decreases from the smallest to the largest ones (Fig. 6B; Table S6). The inclusions are distributed heterogeneously: some grains are inclusion-free, whereas in the other grains up to 4 inclusions are present (Figs. S7A-O, S8; Table S6).

Chromian spinel that hosts PGM cover the full range of chromite compositions thus the presence of PGM inclusions is not meaningfully related to a particular Cr-spinel composition (Fig. 8A). An apparent preference of the SEM-found inclusions to low-Mg# and high-Fe³⁺ Cr-spinel follows from the magnet separation technique utilized to produce Cr-spinel concentrates (see Methods). Occurrence of Pt or Ir-Os inclusions does not correlate with Cr-spinel Mg#, but Ir-Os inclusions seem to be more common in Cr-spinel with lower Fe³⁺/Fe²⁺ (Fig. 8B). Notably, ranges of Ir and Os contents in Cr-spinel surrounding Ir- and Os- bearing inclusions are not different from those in the inclusions-free Cr-spinel (Fig. 8C), suggesting that these inclusions are primary rather than resulted of Ir (Os) exsolution from the host Cr-spinel^{8,20}. Compositions of Pt-Fe alloys weakly depend on the host Cr-spinel as well: weak positive and negative correlations with Cr-spinel Mg# are revealed by Pt and Cu contents in alloys, respectively (Fig. 9A, B). Based on a negative Mg# - Ir correlation in Pt-Fe inclusions from Ambae picrites, Park et al. (2012)²² suggested that these alloys were enriched in Ir during slow cooling and possible re-equilibration between Cr-spinel and olivine, which led to a Mg# decrease. In our case, absence of correlation between Ir (Os) in alloys with Mg# (Fig. 9C, D) is not supportive of this hypothesis and suggests that the compositions of the Tumrok Pt-Fe alloys retain their primary-magmatic features. Thus, the formation of PGM in Tumrok magmas occurred together with the liquidus Cr-spinel along the whole olivine - Cr-spinel cotectic. Furthermore, nucleation and entrapment of PGM by Cr-spinel was sporadic, as some Cr-spinel grains were free of PGM, some are sprinkled with nano-PGM, while others contain rare 0.3–2 μm nuggets.

Cr-spinel PGE budget: admixture vs. PGM inclusions

Data obtained on the PGM inclusions, PGE content of Cr-spinel and the whole rock were combined to calculate the proportions of PGE hosted in each phase. Ranges of PGE admixtures were estimated as their median values ± 1σ. Average amounts of PGE stored in Cr-spinel as PGM inclusions were estimated using surface area data and compositions obtained by SEM (Tables S4, S5), processed through Monte Carlo modelling, and LA ICP-MS data (Table S6). The Monte Carlo modelling was used primarily to estimate the volume (and weight) proportion of the Pt-Fe inclusions in Cr-spinel based on 19 random flat sections across ~10⁵ Cr-spinel grains and showed that this proportion can be calculated using the Delesse principle, which postulates that the areal density of randomly distributed phases in a section tends to their volume density^{35,36}. The modeling accounted for the limited number and actual size distribution of inclusions and demonstrated an accuracy of ~25% (at

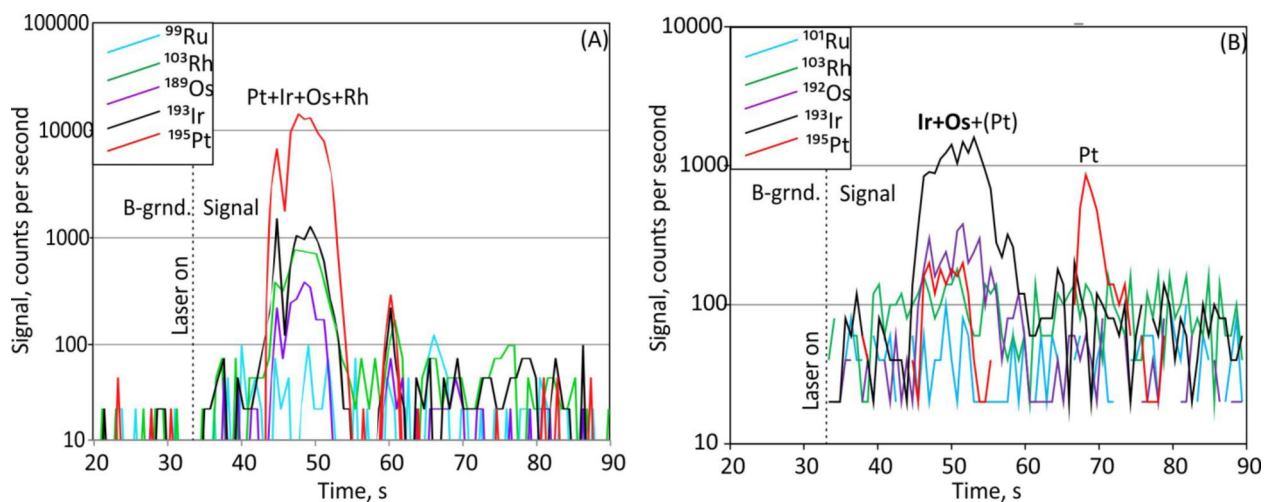


Fig. 7. Time-resolved LA ICP-MS spectra revealing PGE admixture in Cr-spinel and PGM inclusions. **(A)** two Pt-Os-Ir-Rh inclusions of different size; **(B)** an Ir-Os inclusion with minor Pt and a Pt inclusion with possible Ir admixture.

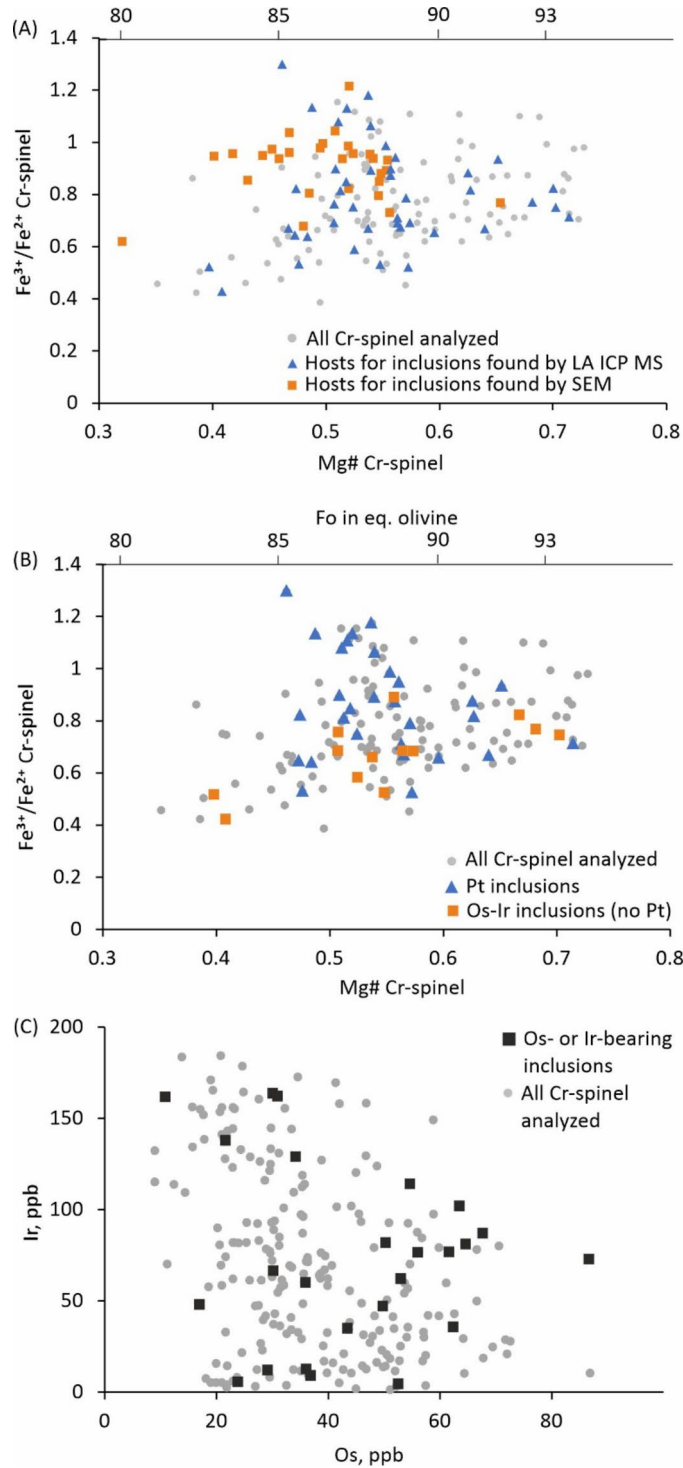


Fig. 8. Binary variation plots characterizing PGM-bearing Cr-spinel compositions compared to all Cr-spinel analyzed from 21AK9c picrite. **(A)** presence and number of inclusions in Cr-spinel; **(B)** particular type of inclusions (Pt-Fe or Os-Ir) in Cr-spinel; **(C)** variations of Os and Ir in Cr-spinel grains with Os-Ir inclusions. Equilibrium forsterite contents in olivine corresponding to the particular Cr-spinel Mg#-s (marked at the upper axes at panels A, B) after Kamenetsky et al. (1995)³⁰.

75% confidence interval) (Fig. 10A). The estimation based on LA ICP-MS data was made by interpreting spike signals to estimate the size of PGM inclusions and summing them across the entire ablated volume of Cr-spinel. More details on SEM- and LA ICP MS-based calculations are discussed in the Methods chapter and presented in Tables S4, S6 and S8.

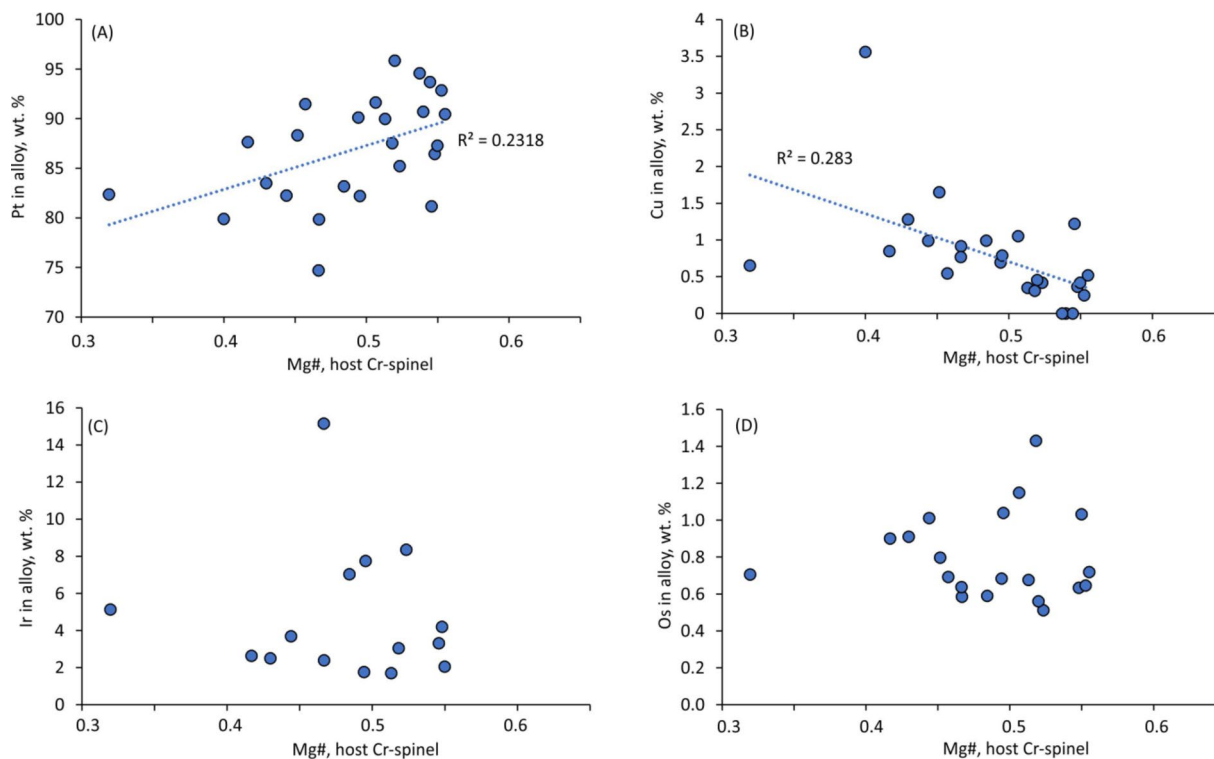


Fig. 9. Chemical variation plots for Pt-Fe alloy inclusions in Cr-spinel. PGE and Cu contents in alloys - EDS data recalculated on Cr-spinel-free basis.

According to these estimations, PGM inclusions account for 100% of Pt, 25–55% (mean 38%) of Os, 12–62% (mean 25%) of Ir and 4–11% (mean 6%) of Rh stored in Cr-spinel (Table S8). Proportion of Ru in the inclusions is negligible as only few nano-sized PGM with Ru have been found; Pd was excluded from consideration due to poor statistics on its content in Pt-Fe alloys. Based on 0.52 wt% Cr-spinel in the 21AK9c picrite, it was calculated (see Methods and Table S8 for the details) that the total amount of PGE accommodated by Cr-spinel – as both chemical admixtures and PGM inclusions – accounts, on average, for 92% of Os, 30% of Ir, 100% of Ru, 56% of Rh and 23% of Pt in the bulk rock (Figs. 3 and 10B; Table S8). Although the uncertainty of this estimation, stemming from variations in PGE admixtures and size distribution of the PGM inclusions is considerable, there is robust evidence that Tumrok Cr-spinel was indeed a principal collector of PGE both as chemical admixtures and PGM (Fig. 3). The contribution of Cr-spinel-hosted admixtures exceeds those estimated for Cr-spinel from some arc, within-plate, and MORB suites²⁰ and the proportion of the bulk rock PGE stored as PGM in Cr-spinel may reach several tens of percent (Fig. 10B).

PGM outside of Cr-spinel

To test whether Cr-spinel (hosting both chemical admixtures of PGE and concentrating PGM nuggets) is the principal control on the PGE behavior, theoretical PGE-Cr trends for Ir, Pt and Rh along the olivine-Cr-spinel cotectic were computed (Fig. 2B, C, D; Table S8). These trends illustrate how PGE should accumulate during crystallization and accumulation of cotectic proportions of olivine and Cr-spinel (98.7 : 1.3) (Fig. 2A) and were calculated based on the calculated bulk contents of PGE in Cr-spinel and LA ICP-MS data for PGE in olivine. The trends were calculated for the two scenarios. In the first scenario (red dashed lines and pink fields in Fig. 2B–D), we assumed that PGE are concentrated exclusively in Cr-spinel (as admixture and PGM inclusions), while olivine contains no PGE. Red dashed lines represent trends calculated for average total contents of PGE in Cr-spinel; pink fields cover ranges between calculations based on lower and upper limits of the estimation of these contents (Table S8). The second scenario represents the maximum possible accumulation of PGE (grey dashed lines at Fig. 2C, D), we suggest that Cr-spinel contains the highest possible PGE amounts (upper limits of the estimations) and the PGE contents in olivine are as high as the detection limits of LA ICP-MS since the measured PGE concentrations in olivine were below these detection limits (Table S8).

The Rh-Cr trend range overlaps with that formed by picrite compositions (Fig. 2B) thus indicating that crystallization of Cr-spinel containing PGE admixtures and PGM inclusions explains the accumulation of Rh in a putative olivine - Cr-spinel cumulate. By contrast, the Cr-Ir and Cr-Pt calculated trends do not overlap with the real trends formed by picrite compositions, even when the highest possible PGE content is assigned to olivine (Fig. 2C, D). A steeper increase in these elements with accumulation of Cr-spinel and olivine suggests that there should be additional and significant factor enriching and fractionating Cr-spinel + olivine assemblage in these PGE. Since concentration of both these elements in olivine and clinopyroxene is low (Table S3) and clinopyroxene does not accumulate along with olivine, it is implied that PGM are not exclusively hosted by Cr-

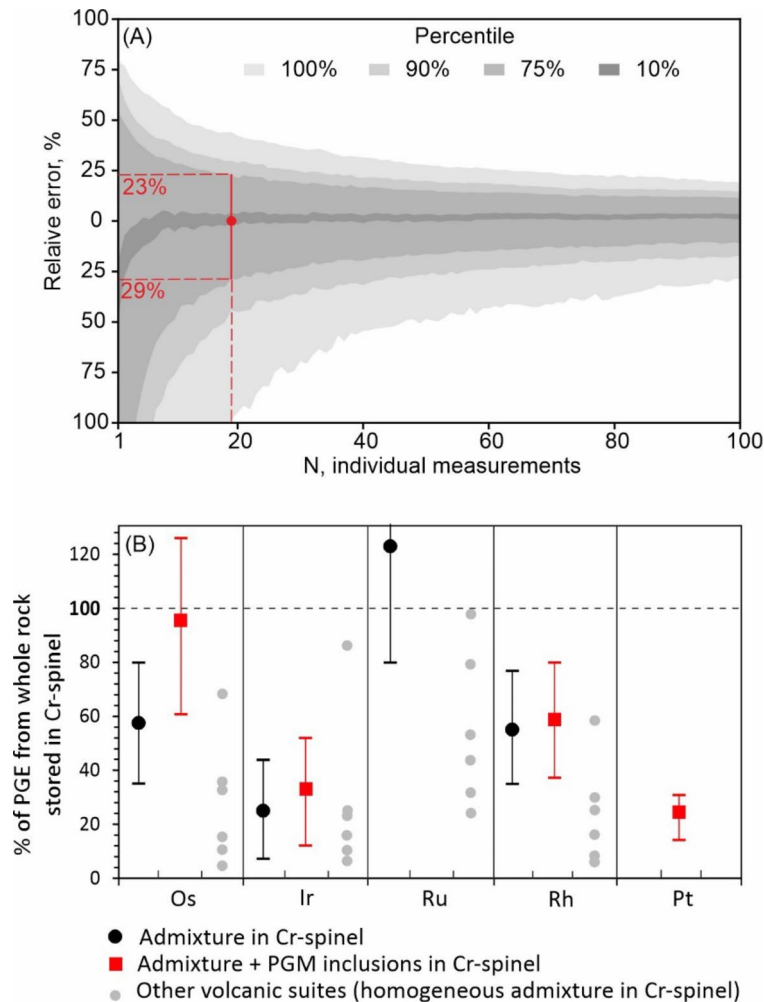


Fig. 10. Results of calculation of contribution of PGM hosted by Cr-spinel in the whole rock budget. (A) distribution of relative errors (uncertainty) for the estimation of integral Pt-Fe alloy/Cr-spinel volume ratio based on Delesse principle applied to the flat section of Cr-spinel-hosted Pt-Fe inclusions: results of the Monte Carlo modelling (see Methods for details). The X axis refers to the number of the inclusions used for the calculation. The Y axis refers to a relative error of such a calculation. The error is the ratio of the Delesse-based estimation of the alloy/Cr-spinel value to the “real” alloy/Cr-spinel value, pre-defined in a statistical computer experiment. The grey fields show probability density of the error with the percentiles given in the legend. The uncertainty range of +23 and –29% at 75% percentile is highlighted for 19 individual Pt-Fe inclusions measured in this study. (B) Results of mass balance calculations showing the proportion of the PGE in the whole-rock that comes from the contribution of (1) PGE admixture in Cr-spinel only (black points) and (2) total contribution of PGE admixture + PGM inclusions in Cr-spinel (red points). Grey points corresponding to contributions of PGE admixture in Cr-spinel in the whole-rock from various volcanic occurrences worldwide are from Pagé and Barnes²⁰. Error bars for the points corresponding to PGE admixture in Cr-spinel are given as 1 SD. Error bars for the points corresponding to PGE admixture + PGM inclusions are given as 1 SD of PGE admixture plus errors of the PGM area calculation normalized to the mean content of a particular PGE in Pt-Fe alloys (see “Methods” for the details).

spinel. A significant portion of the PGM may be included in olivine or attached to crystal surfaces, as shown experimentally by Ballhaus et al.²⁷ who reported that submicron PGM particles settle on crystal surfaces, particularly on Cr-spinel grains, and geochemical data on picrites and komatiites^{17,20}. In addition, our estimate may underestimate the true quantity of PGM hosted by Cr-spinel due to the “nugget effect”. (see below in ‘Methodological advances’).

That Cr-spinel is not the major host of Ir during early-magmatic crystallization of primitive magmas is also inferred from comparison between Cr-Ir trends formed by Tumrok picrites and low-Ti picrites of Emeishan¹⁰. The correlations observed in those series are almost the same (Fig. 2C), while empirical $K_d^{\text{Chr/melt}}$ (Ir) calculated for them are contrasting: 328 (Table S8) for Tumrok and 27 for Emeishan¹⁰. Such a discrepancy provides an additional (and independent of our model calculations) support to the suggestion that although Cr-spinel control on Ir – and possibly other IPGE – is important, there should be some other phase, probably PGM, determining Ir behavior along olivine – Cr-spinel cotectic.

Origins of PGE scattering: nuggets and local effects

Our data support earlier contention that liquidus Cr-spinel is a significant reservoir of PGE both as chemical admixtures^{17–23} and PGM inclusions^{5,22,24–28}. In addition, they demonstrate irregular relationships between PGE abundances, ratios, and PGM occurrence and composition, with respect to crystallization degree, host Cr-spinel major element composition, and a redox record by Cr-spinel ($\text{Fe}^{3+}/\text{Fe}^{2+}$ ratio). There are a multitude of factors controlling PGE partitioning and solubility in sulfide-undersaturated melts and below we consider in detail some of them.

The PGE content of Cr-spinel is mainly controlled by its concentration at the Cr-spinel–melt boundary layer, redox conditions and Fe^{3+} proportion in Cr-spinel^{18,20}. These factors may vary locally and rapidly around a growing Cr-spinel crystal. Redox is controlled by $\text{Fe}^{2+}/\text{Fe}^{3+}$ gradient at the boundary layer, which depends on the rate of a crystal growth. Furthermore, Brenan et al. (2012)¹⁸ calculated that an increase of $\text{Fe}^{3+}/(\text{Fe}^{3+} + \text{Cr})$ in Cr-spinel from 0.1 to 0.3 increases the partitioning coefficients for Ir and Rh between Cr-spinel and melt up to 1.5 orders of magnitude. This is assumed to result from the inversion of the spinel structure and creating VI-fold vacancies, enhancing entrance of Ru^{2+} and Ir^{2+} ¹⁸. In our case, $\text{Fe}^{3+}/(\text{Fe}^{3+} + \text{Cr})_{\text{Cr-spinel}}$ values vary mainly between 0.12 and 0.3 and, hence, these variations may account for the observed scattering in Ir and Rh contents in Tumrok Cr-spinel, yet it is unclear why Rh correlates with Fe^{3+} while Ir does not (Fig. 4A, B). The erratic behavior of Os may be partially attributed to its sensitivity to degassing which is implied by its elevated contents in volcanic emanations³⁷. Thus, if a Cr-spinel crystal were attached to a fluid bubble^{38,39} or a degassing took place in a restricted batch of magma, then the Os concentration could be affected by partitioning of PGE into the fluid.

The fact that early-magmatic PGM are important PGE reservoirs and are not restricted to Cr-spinel, implies that so-called “nugget effect” may significantly disturb bulk rock PGE systematics. Size (and, hence, mass) distribution of Cr-spinel-hosted PGM shows that although 30 to 300 nm Pt-Fe inclusions are common, they are insignificant repositories of Pt (< 5%) compared to rarer but larger nuggets (> 500 nm) (Table S8). Specifically, among ~60 studied inclusions, the largest found Pt-Fe alloy inclusion (~3 μm across) (Fig. S6L; Table S4) accounts for 1/3 of total Pt in Cr-spinel, according to our calculation. This further highlights that ‘size matters’ and that a single large PGM may strongly affect PGE content in single rock sample. It is possible that the nugget effect is responsible for elevated Os, Ir and Pt in some basalts from the studied suite (Fig. 2C, D; Fig. S3D).

On a local scale, formation of PGM at the Cr-spinel – melt boundary layer is strongly controlled by the redox shift⁹: fast Cr-spinel growth producing a sharp $\text{Fe}^{3+}/\text{Fe}^{2+}$ gradient at the boundary layer is favorable for the PGM formation as it locally reduces $f(\text{O}_2)$ and decreases solubility of PGE alloys^{5,40}. Furthermore, local fluctuations of Fe concentrations, which occur around growing Cr-spinel should also increase or decrease solubility of the Pt-Fe alloys⁴¹. These kinetic factors, in turn, control rates of nucleation and crystallization of PGM and their variations in disequilibrium conditions may account for a broad dispersion of the PGM sizes. Sulfur fugacity is known to control crystallization of PGM sulfides, primarily laurite (RuS_2)–erlichmanite (OsS_2) series^{42,43} but given the absence of these minerals in the studied case, we here do not discuss this factor further. Finally, nano-to-microscale particles of metal alloys in silicate melt readily attach to fluid bubbles (Fig. 5 in³⁸). Thus, local degassing events may be important in remobilizing and collecting of PGM.

The discussed factors controlling PGE partitioning into Cr-spinel and PGM crystallization appear to be competitive and exhibit opposing dependence on redox and, to some extent, degassing. Melt oxidation increases solubility of the PGE alloys^{5,40,41} and, hence, may inhibit nucleation and crystallization of PGM. Conversely, it increases chemical K_d of PGE between Cr-spinel and melt. Reduction of the melt has the opposite effect on both alloy solubility and PGE partitioning. Degassing may scavenge Os from the melt, thereby decreasing its concentration in crystallizing Cr-spinel, while fluid bubbles may collect PGM that crystallized prior to the degassing³⁸. Therefore, the interplay between PGE incorporation into Cr-spinel and PGM formation introduces further complexity into their behavior in primitive magmas.

A key remaining question is: if PGE behavior depends on redox conditions during Cr-spinel crystallization, why are PGE contents and PGM occurrence poorly correlated with Fe^{3+} content in Cr-spinel? Although this contradiction remains unresolved, we tentatively suggest that being highly sensitive to a redox fluctuations, IPGE and Rh may form local enrichments (e.g. thin zones) in a growing Cr-spinel due to redox fluctuations in a boundary layer produced by kinetic effects. In this case, Fe^{3+} measured even near the laser ablation pit by EPMA may not reflect this particular zone or, possibly, diffusion rate of Fe^{3+} in Cr-spinel was high enough to erase fine zoning of this ion. Similarly, a PGM crystallized at a given moment of a Cr-spinel growth may reflect a very local and relatively rapid change of the conditions at the boundary layer, while major component composition of Cr-spinel is representative more of the average conditions over the crystal’s growth period. Overall, local kinetic effects during Cr-spinel growth appear to be among the key reasons for the erratic behavior of PGE revealed in this study, opening further perspectives for studying of PGE and PGM in Cr-spinel using local approaches such as TEM and atom probe microscopy^{44–46}.

Methodological advances

To quantify PGE behavior in sulfide-undersaturated magmas, we used a combined approach to study PGE systematics in volcanic rocks. The details, including computational algorithms and formulae, are provided in the Methods; here we briefly discuss the approach’s principal advantages and limitations compared to existing methods. Existing approaches, briefly summarized by Mina and Anenburg⁹ and applied mostly to plutonic rocks utilize: (1) bulk geochemical methods for detecting PGE and Au at sub-ppb levels⁴⁷; (2) optical and electron microscopy^{48,49}; (3) LA ICP MS, that allows for analyzing noble metal admixtures in sulfides^{50,51}, Cr-spinel²³ as well as to find micro- and nano-inclusions of PGM in these minerals^{21,22,50,52}; (4) X-ray tomography⁵³ and atom probe tomography⁴⁵ showing spatial distribution and prevalence of the PGM species in a particular volume of a sample; (5) automatized 2D mineralogical analysis allowing for a precise and time-saving estimation of the

PGM prevalence and in a particular rock⁵⁴. Combining these methods has been shown to increase effectiveness of studying PGE geochemistry and ore-forming processes^{9,55}.

When applied to volcanic rocks, combining bulk rock chemistry with spot LA-ICP-MS has proven effective for quantitative assessment of role of Cr-spinel in PGE geochemistry in picritic, komatiitic and basaltic suites^{20–23}. Here, we further develop by incorporating statistical data on Cr-spinel-hosted PGM acquired by a search of PGM and estimation of their size by both LA ICP MS and automatized SEM techniques. Laser ablation ICP MS reveals PGM inclusions larger than ~ 30 nm as spikes on the time-resolved ICP MS spectra and allows estimation of their element composition and roughly quantify their size if the PGE content in a host mineral and laser beam diameter are known (see Methods for the calculation details). Automatized SEM EDS analysis of the mineral concentrates containing thousands of grains allows for finding tens of larger (> 200 nm) but rarer PGM inclusions with their subsequent spot chemical analysis and area measurements. From these area measurements, the volume and mass proportions of the inclusions relative to the host minerals are derived. Monte Carlo simulations show that for isoferroplatinum inclusions in volcanic Cr-spinel, more than 15 individual inclusions are sufficient to estimate their mass proportion to the host mineral with a precision of ± 50% (see Methods for the calculation details).

The proposed combined approach has important limitations, the most significant being the notorious “nugget effect”. Even though searching of PGM inclusions over thousands of Cr-spinel grains provides a statistical dataset, the size distribution of the PGM is heterogeneous with the largest and rarest inclusions accounting for most of PGE in a rock (see above). Hence, although in this study we deduce that only 25% of Pt in the rock is stored as Cr-spinel-hosted Pt-Fe inclusions, we cannot rule out that a single large nugget which did not occur within the selection holds the remaining 75%. To overcome this limitation, a complete 3D scanning of a hand sample (or at least Cr-spinel concentrate) with ~ 100 nm resolution would be needed, which remains technologically challenging. Thus, our step towards quantifying behavior of PGE in sulfide-unsaturated volcanics shows that PGE remain elusive and only semi-quantitative estimations are currently possible. Other issues include an uncertainty in the LA-ICP-MS based volume estimations and time-consuming search of the PGM by SEM EDS (which still gains low statistics with only 19 PGM identified per section so far). Nevertheless, the case study of the oxidized arc picritic-basaltic suite of the Tumrok range (Eastern Kamchatka) shows that such semi-quantitative exercises, if applied carefully, enable valuable new insights into geochemistry of PGE and, potentially, other rare elements in volcanic rocks.

Concluding remarks

Platinum-group element systematics in volcanic rocks of the Tumrok range indicate that Cr-spinel concentrates all PGE except Pd. Statistical analysis of the PGM inclusions in Cr-spinel enabled the first numerical evaluation of the proportion of PGE stored as PGM in volcanic rocks and highlighted the importance of the “nugget fractionation”²⁷ of PGE in sulfide-unsaturated primitive magmas. It showed that the behavior of PGE in sulfide-unsaturated systems is complex and, in some sense, stochastic. First, partitioning of PGE into Cr-spinel varies extremely (~ 2 orders of magnitude) even within a single sample, despite being reported to correlate with Fe³⁺ proportion^{18,22,23}. PGE contents in Cr-spinel may be actually poorly dependent on Cr-spinel composition and uncorrelated with one another. Second, the importance of PGM in PGE systematics, along with > 2 orders of magnitude size variation, underscores the significance of the nugget effect in bulk rock PGE compositions. Both partitioning of the PGE and PGM crystallization depend on a number of conditions (including but not restricted to PGE content in melt, redox conditions, Fe content and presence of fluid), which are readily susceptible to local variations, particularly – around crystallizing Cr-spinel. Furthermore, PGM crystallization and chemical partitioning of PGE in Cr-spinel are competitive and contrariwise depend on $f(\text{O}_2)$. The interplay of these local factors and the nugget effect may result in a broad variation of PGE partitioning even within the same magma batch making their behavior in a bulk system complex and erratic.

Methods

In this chapter, instrumental analytical techniques are described in brief (see Supplementary Information and Tables S9–S11 for details of the analytical protocols), whereas approaches for the estimation of the role of PGM in PGE partitioning are disclosed in detail.

Analytical techniques

For the bulk rock PGE analysis, the samples were crushed in an Al-ceramic mill to 200 mesh. Platinum-group elements and Au concentrations were determined on 15 g of the powder by Ni-fire assay Te-co-precipitation and inductively coupled plasma mass spectrometry analysis following the method of⁴⁷ in LabMaTer Université du Québec Chicoutimi. Results for the reference materials OKUM/GeoPt 20 (a komatiite), LK NIP1 (a diabase) WGB1 (a gabbro) and TDB1 (a diabase) agree with certificate values (Table S9).

Scanning electron microscope images (except high-magnification photos of PGM inclusions) were obtained by Tescan Vega 2 microscope at Korzhinskii Institute of Experimental mineralogy RAS (Chernogolovka, Russia). Quantitative major and trace-element (except PGE) analyses of Cr-spinel were carried out using JEOL JXA-8530 F Plus field emission electron probe microanalyser in University of Tasmania (UTAS) (Australia) (accelerating voltage 15 kV, beam current 40 nA) and JEOL JXA-8230 electron probe microanalyser in Laboratory of Local Methods of Matter Study, Department of Geology, Moscow State University (MSU) (Russia) (accelerating voltage 20 kV, beam current 70 nA). Natural and synthetic minerals and oxides were used as primary and secondary reference materials during EPMA analysis (Supplementary Information).

Laser ablation ICP-MS analyses of major, trace and platinum group elements (PGE) were carried out on Cr-spinel at the LA-ICP-MS laboratory of the Collaborative Innovation Center for Exploration of Strategic Mineral

Resources, China University of Geosciences (CUG), Wuhan, China; on olivine, clinopyroxene and serpentine in CODES Analytical Laboratories, University of Tasmania. Laser ablation ICP MS without quantification of the raw data, to gain statistics on the PGM inclusions in Cr-spinel, was carried out in Institute of the Earth's Crust of the Russian Academy of Sciences (Irkutsk, Russia).

LA-ICP-MS analysis at CUG has used a quadrupole Agilent 7900 ICP-MS coupled to TwoVol3 ablation cell and 193 nm wavelength laser (NWR 193 HE, New Wave Research). The ablation was conducted in He flowing at 0.55 l/min, which was mixed with Ar flowing at 0.38–0.5 l/min. The oxide production rate was <0.5% and doubly charged ions <0.3%. The analyses were performed by a laser beam spot 50–100 μm with a repetition rate 5–10 Hz. The laser fluence, determined by an external energy meter, was $\sim 3 \text{ J}/\text{cm}^2$. The list of measured isotopes included ^{24}Mg , ^{27}Al , ^{29}Si , ^{49}Ti , ^{53}Cr , ^{57}Fe , ^{59}Co , ^{60}Ni , ^{63}Cu with dwell time 0.006 s and ^{99}Ru , ^{101}Ru , ^{103}Rh , ^{185}Re , ^{189}Os , ^{193}Ir , ^{195}Pt with dwell time 0.06 s. This allowed to increase fraction time dedicated to measurement of PGE to about 84% of the sweep time. The gas background was recorded for 30 s before each measurement and signal was accumulated for 40 s. Synthetic and natural glasses, sulfides and oxides were used as primary and secondary reference materials (Supplementary Information and Table S10). Pure Ni, Co and Cu metals were measured during the session for estimation of the production of argide interferences: $^{61}\text{Ni}^{40}\text{Ar}$ to $^{101}\text{Ru}^{63}\text{Cu}^{40}\text{Ar}$ to $^{103}\text{Rh}^{65}\text{Cu}^{40}\text{Ar}$ to ^{105}Pd . The data reduction was conducted using LADR software⁵⁶ version 1.1.7.0 and the composition of Cr-spinel was calculated by normalization to total sum of oxides assuming all iron as Fe^{2+} . The estimated detection limits were ~ 3 ppb for Pt and Re, 4–6 ppb for Pd, 2–10 ppb for Os, 1–4 ppb for Ir, 1–6 ppb for Rh, 15–30 ppb for Ru and 1–3 ppb for Au.

Spot LA-ICP-MS analyses at CODES Analytical Laboratories, University of Tasmania were performed on ASI RESOLUTION-SE-S155 laser microprobe equipped with an ATL ATLEX 193 nm Ar-F excimer laser, coupled to an Agilent 7900 quadrupole ICP-MS. A laser beam size of 40 μm was used with a pulse rate of 5 Hz and a laser fluence of 3.5 J/cm^2 . Ablation was performed in a He atmosphere flowing at 0.35 l/min. The ablated aerosol was mixed with Ar (1.05 l/min) as a transport gas, before exiting the cell. The isotopes measured in minerals and the primary and secondary standards were: ^{24}Mg , ^{27}Al , ^{29}Si , ^{34}S , ^{43}Ca , ^{47}Ti , ^{51}V , ^{53}Cr , ^{55}Mn , ^{57}Fe , ^{59}Co , ^{60}Ni , ^{65}Cu , ^{66}Zn , ^{75}As , ^{77}Se , ^{88}Sr , ^{90}Zr , ^{99}Co , ^{99}Ru , ^{101}Ru , ^{103}Rh , ^{105}Pd , ^{106}Pd , ^{107}Ag , ^{111}Cd , ^{125}Te , ^{157}Gd , ^{185}Re , ^{189}Os , ^{193}Ir , ^{195}Pt , ^{197}Au , ^{208}Pb and ^{209}Bi . Dwell times were 0.002 s for Mg, Al, Si, Ti, V, Mn, Sr, Zr and Gd; 0.005 s for S, Ca, As, Se, Cd, Te, Pb and Bi; 0.01 s for Fe, Co, Ni, Cu, Zn and Ag and 0.03 s for all other elements, resulting in a total sweep time of 0.487 s. Total acquisition time for each analysis was 90 second, consisting of a 30 s gas background and 60 s ablated signal. Synthetic and natural glasses, sulfides and oxides were used as primary and secondary reference materials (Supplementary Information and Table S11). Data reduction was done according to the methods established by Longrich et al.⁵⁷ using LADR software⁵⁶. Quantification was performed using ^{57}Fe as the internal standard element, normalizing all measured cations to the oxide total of 100%. Correction factors for base metal-argide interferences on Ru, Rh and Pd were obtained by ablating pure Ni, Cu, Zn and Co metals.

Additional search for the PGM inclusions as spikes in the time-resolved laser ablation spectra (without recalculation of the raw signal to the concentrations) has been performed by the LA ICP-MS facility of the Institute of the Earth's Crust of the Russian Academy of Sciences (Irkutsk, Russia): quadrupole mass-spectrometer Agilent 7900 coupled to Analyte Excite (Teledyne Photon Machines) laser ablation system with the HelEx II ablation cell and excimer laser ArF 193 nm. The ablation was conducted in He flowing at 1.0 l/min, which was mixed with Ar flowing at 1 l/min. Argon was used as cooling and plasma gas at the flow rates of 16.0 and 1.0 l/min correspondingly. Spot analyses have been performed at beam diameter 110 μm , frequency 10 Hz, and power 3.5 J/cm^2 . The signal was measured for 60 s, the background – for 30 s. Dwell time for noble metals (^{101}Ru , ^{103}Rh , ^{105}Pd , ^{192}Os , ^{193}Ir , ^{195}Pt and ^{197}Au), ^{34}S , ^{75}As , ^{125}Te was 0.05 s, for major components ^{24}Mg , ^{29}Si , ^{57}Fe – 0.01 s, for transitional metals – 0.02 s ^{47}Ti , ^{66}Zn and 0.05 s ^{59}Co , ^{60}Ni , ^{63}Cu . Total sweep time was 0.750 s.

Automated search and analysis of PGM inclusions in Cr-spinel

For the search and analysis of the Cr-spinel-hosted microinclusions of PGM, Cr-spinel concentrates were produced from 21AK9c and 21AK17 samples by crushing them to the fraction <0.2 mm with subsequent gravitational and magnetic separation. Because of high Fe content, >90% of Cr-spinel grains turned to be in the weakly-magnetic fraction, separated by a neodymium magnet. The concentrates produced contained $\sim 60\%$ of Cr-spinel, $\sim 30\%$ of magnetite and $\sim 10\%$ of olivine. The concentrates were mounted into epoxy mounts, grinded and polished using water-free lubricant and diamond abrasives. Two mounts were made for the 21AK17 sample and three – for the 21AK9c sample. An order of 10^4 of individual Cr-spinel grains were exposed in each mount (Fig. S9).

Mounts with concentrate from 21AK17 were manually “scanned” on Tescan Mira 3 LMU microscope (Analytical Center for multi-elemental and isotope research, Siberian Branch of Russian Academy of Sciences, Novosibirsk, Russia – ACMEIR SB RAS) with a field of view $\sim 500 \mu\text{m}$, which allowed for identification of bright PGM phases down to 0.25 μm in size because excitation area of these phases was broader than the apparent size and they were visible at this magnification.

Mounts with concentrate from 21AK9c were scanned using Tescan Mira with TESCAN Integrated Mineral Analyzer (TIMA)⁵⁸ scanning electron microscope in Central Research Institute of Geological Prospecting for Base and Precious Metals (TSNIGRI), Moscow, Russia. The approach is based on scanning of the sample by a 0.1 μm beam with a 0.5 μm step, which (1) finds phases with BSE-brightness exceeding that of magnetite and (2) acquires EDS spectra from those phases to test whether they contain Pt. Beam voltage was 25 kV, beam current – 0.1 nA, detector model - PulseTor 30 (EDAX Element 30 in compatibility mode), average excitation area – 0.1 μm depending on a mean atomic weight of the analyte. This approach guaranteed identifying Pt-Fe alloys with size of at least 0.5 μm (real limit was 0.25–0.3 μm according to our data).

High-resolution imaging and semi-quantitative spot analyses of PGM inclusions in Cr-spinel were carried out by Tescan Mira 3 LMU scanning electron microscope equipped with INCA Energy 450 XMax 80 microanalysis

energy-dispersive system at the ACMEIR SB RAS, Novosibirsk, Russia. Accelerating voltage was 20 kV, a beam current – 1.6 nA, a detector energy resolution of 126–127 eV at the Mn K α line. Excitation area was ~ 3 μ m depending on the average atomic weight of the analyte. The live time of spectrum acquisition was 60 s. As the main X-ray lines of Rh and Ru are overlapping, we attributed the signal to Rh in all cases, because Ru was not present in the inclusions according to LA ICP-MS data. All analyses obtained from the PGM inclusions in Cr-spinel represented a mixture between the PGM and the host Cr-spinel, thus the raw data was recalculated subtracting “Cr-spinel input” estimated from Cr content in the analysis and composition of the host Cr-spinel. Detection limits, estimated as 3 σ of the signal/noise ratio varied from analysis to analysis and were, on average, 0.1–0.2 wt%; errors (2 σ) were lower than 0.2–0.3 wt% for the major elements and 0.1 wt% for the minor elements.

Estimation of the PGE stored as PGM in Cr-spinel: based on surface area of the exposed inclusions

This estimation is based on the Delesse principle^{35,36} postulating that volume proportion of two phases equals their area proportion among all possible sections of the volume, provided that their relative distribution is random and homogeneous. In the case studied, nearly-octahedral Cr-spinel and nearly-cubic Pt-Fe alloys can be considered equidimensional, thus no correction on their different shape should be applied. Surface area of Pt-Fe alloys in three mounts from 21AK9c (19 inclusions) (Fig. 5A, Fig. S6A-S) has been measured in ImageJ and INCA Atlas software (Fig. S6A, Table S4). Total surface area of Cr-spinel in an epoxy mount was estimated in two steps. First, the high-resolution panoramic back-scattered electron image of a mount (Fig. S9A) was processed in Adobe Photoshop to recolor Cr-spinel grains using brightness levels adjustment and the “Gradient Map” tool (Fig. S9B). Second, the image with Cr-spinel grains recolored was processed in INCA Atlas software to extract area proportion of the color assigned to Cr-spinel at the raster. Given the mount radius known, surface area of the Cr-spinel in a mount has been quantified (Table S4). A ratio between the total surface of Pt-Fe alloys and the total surface of Cr-spinel, multiplied by a coefficient accounting for the stoichiometry and densities of Pt-Fe alloys and Cr-spinel, was taken as the estimation of content of Pt stored as inclusions in Cr-spinel (Table S4).

However, we deal with a strongly restricted set of Pt-Fe alloy sections dispersed within an overwhelming volume of Cr-spinel. Therefore, it must be tested whether the Delesse principle is applicable in the particular case or the errors arising from the area differences and lack of the statistics make this estimation senseless. This test has been performed by statistical modelling based on distribution of inclusions over their random plane section. The script was designed in Python 3.8 Spyder IDE programming medium and is available via https://github.com/SergeyEKonstantinov/RelArea_estimator.git. First, we introduced the solid three dimensional medium (corresponding to a Cr-spinel matrix) as its flat unfolding that we rearranged to a square with integer side M . Each of M^2 positions of this medium can be occupied by an inclusion randomly picked from the distribution with probability p . From the real ratio of Pt-Fe to Cr-spinel areas in our sections - $p \approx 1.7 \cdot 10^{-7}$. Then we introduced the “pre-known” value of relative area of inclusions in each unfolding A_{true} and settled the “inclusions” randomly with parameters p and A_{true} within the medium. After this, a random slice of medium, which is a square region with such side length l that occupies exactly N inclusions, was picked. After the pick, we calculated the relative area of the inclusions over l^2 . This random slice picking was repeated for 10^3 times per N , so a distribution of relative areas for each N has been obtained. This whole process was repeated and averaged over 10 randomly generated unfoldings and normalized to A_{true} to represent the relative error. We first constructed the relative areas error plot for a distribution of random unit cube sections (Fig. S10A) obtained in Hull and Houk⁵⁹. The plot shows that this distribution is nearly-symmetric and for $N=19$ 75% of numerical occurrences lie within 10% interval (Fig. S10A). Then a new distributed factor based on the observed size distribution (Fig. 6A; Table S4) was introduced using Gaussian kernel density estimator. The uncertainty increased significantly due to variation of the inclusions’ sizes and is (+23 -29%) for the 75% percentile (Fig. 10A; Fig. S10B). Notably, the error distribution based on the real size distribution is asymmetric towards a negative error due to the cases of high sectional area (almost 10 times the mean) resulting in a possible overestimation of the model and reiterating the importance of the “nugget effect”.

Estimation of the PGE stored as PGM in Cr-spinel: based on PGE spikes in LA ICP-MS spectra

From the PGE spikes on the laser ablation spectra, relative mass (and, hence, volume) proportions of the inclusion and the ablated host can be roughly estimated^{60,61}. Using these parameters (Fig. S11), an average content of a PGE stored as inclusions is found in three steps: (1) obtain the total volume of the inclusions, (2) divide it by the total volume ablated and (3) multiply by the coefficient, characterizing the density difference between inclusion and the host.

For the case of Pt-Fe inclusions, Pt content in the host Cr-spinel can be taken as zero, so the calculation will be as below:

(a) set volume ratio of Pt-Fe alloy and host chromite in the ablated volume as

$$\frac{V_{PtFe}}{V_{Chr}} = \frac{m_{Pt}}{0.9\rho_{PtFe}} / \frac{m_{Cr}}{0.34\rho_{Chr}} \quad (1)$$

where m_{Pt} and m_{Cr} are masses of platinum and chromium in the ablated volume, 0.9 and 0.34 are average mass proportions of Pt and Cr in isoferroplatinum and Cr-spinel, respectively. For a given ablated volume, ratio of masses equals ratio of concentrations, thus

$$\frac{V_{PtFe}}{V_{Chr}} = \frac{C_{Pt}}{0.9\rho_{PtFe}} / \frac{C_{Cr}}{0.34\rho_{Chr}}, \quad (2)$$

where C_{Pt} and C_{Cr} are concentrations, rendered for a given LA ICP MS spike (Table S6).

(b) Ablated volume, signal from which contains the PGE spike, is calculated as:

$$V_{drilled} = \frac{T_i}{T_0} h \pi \left(\frac{D}{2} \right)^2 \quad (3)$$

where T_i and T_0 are durations of the PGE spike and total time of the spot ablation (60 s), respectively, h is the depth of a pit ($\sim 15 \mu\text{m}$ as measured by focusing of an optical microscope), D is the diameter of a pit.

(c) Assuming that the inclusion size is negligible compared to the volume ablated,

$$V_{PtFe} = \frac{T_i}{T_0} h \pi \left(\frac{D}{2} \right)^2 \times \frac{C_{Pt}}{0.9 \rho_{PtFe}} / \frac{C_{Cr}}{0.34 \rho_{Chr}} \quad (4)$$

(d) Summing the volumes of all found Pt-Fe inclusions and taking all constants (densities and stoichiometric coefficients, ablation depth and total time ablated) from the summation sign:

$$V_{PtFe}^{total} = \frac{0.34 \rho_{Chr} \times h \pi}{0.9 \rho_{PtFe} \times 4 T_0} \sum_{i=1}^n \left(\frac{C_{Pt}^i}{C_{Cr}^i} T_i D_i^2 \right) \quad (5)$$

where i is number of inclusions.

(e) Similarly, total volume ablated is

$$V^{total} = \frac{\pi h}{4} \sum_{k=1}^m D_k^2 \quad (6)$$

where m is the number of spots ablated.

(f) From the Eqs. (5) and (6), mass ratio of all Pt-Fe inclusions to all ablated Cr-spinel is

$$\frac{m_{PtFe}}{m_{total}} = \frac{\rho_{PtFe}}{\rho_{Chr}} \times \frac{0.34 \rho_{Chr} \times \pi h \sum_{i=1}^n \left(\frac{C_{Pt}^i}{C_{Cr}^i} T_i D_i^2 \right)}{\frac{\pi h}{4} \sum_{k=1}^m D_k^2} = \frac{0.34}{0.9 \times T_0} \frac{\sum_{i=1}^n \left(\frac{C_{Pt}^i}{C_{Cr}^i} T_i D_i^2 \right)}{\sum_{k=1}^m D_k^2} \quad (7)$$

from which concentration of Pt stored as Pt-Fe inclusions in Cr-spinel can be found given that an average Pt content in a Pt-Fe alloy in our case is $\sim 90\%$.

$$C(Pt) = \frac{m_{Pt}}{m_{total}} = \frac{0.34}{T_0} \frac{\sum_{i=1}^n \left(\frac{C_{Pt}^i}{C_{Cr}^i} T_i D_i^2 \right)}{\sum_{k=1}^m D_k^2} \quad (8)$$

Notably, concentration of a PGE in the inclusion is reduced in this equation, thus the final value does not depend on the exact content of a PGE in the inclusions.

Equation estimating Os, Ir and Rh contents stored as PGMs (native metals) is similar to the above one, but takes into account the crystallochemical content of these metals in Cr-spinel. The latter was calculated by an integration of the time-resolved LA spectra excluding the spike corresponding to a PGM inclusion.

$$C(Os) = \frac{m_{Os}}{m_{total}} = \frac{0.34}{T_0} \times \frac{\sum_{i=1}^n \left(\left(\frac{C_{OsMix}^i - C_{OsHost}^i}{C_{Cr}^i} \right) T_i D_i^2 \right)}{\sum_{k=1}^m D_k^2} \quad (9)$$

where C_{OsMix} is measured concentration of Os in the spike, C_{OsHost} is concentration of Os in the host Cr-spinel (rendered from the LA ICP MS signal excluding the spike). Calculations for Ir and Rh were carried out in the same way, while Ru was not estimated due to scarcity of Ru-bearing inclusions. The calculation procedure is written as the MScExcel formulae in Table S6.

Comparison between the approaches based on surface area and LA ICP-MS

Characteristic dimensions of the PGM inclusions estimated from LA ICP-MS data vary between 20 and 300 nm, while dimensions of those found by SEM are 0.2–3.3 μm (Fig. 6; Tables S4, S6). As an explanation for such an apparent discrepancy, it is suggested that these methods cover different fractions of sizes of the inclusions. Laser ablation ICP MS, performed on ~ 160 Cr-spinel grains, allowed to detect smaller, but more abundant inclusions, while SEM examination, covering 10^4 – 10^5 grains found larger, but rare inclusions. According to a simple geometrical consideration, if laser ablation depth is 15 μm , then a 0.5 μm isometrical nugget, which occurs in 1 of 5000 flat sections of Cr-spinel with average grain size of 0.1 mm will be found in ~ 1 of 170 LA spots ablated by 100 μm beam and in ~ 1 of 680 spots ablated by a 50 μm beam. This estimation is roughly coincident with the obtained data showing that the largest PGM found by LA ICP-MS over ~ 160 Cr-spinel grains has a characteristic dimension of 280 nm (Table S6).

Another complication with the LA ICP MS based approach is that it does not allow for a precise size estimation of inclusions, particularly of those which spikes occupy few sweeps and, thus, have low statistics on a signal intensity. Furthermore, a precise estimation of the particle size by LA ICP-MS needs calibration coefficients determined on specific “particle standards”⁶¹. Nevertheless, by now, this is the only approach to

find < 0.25 μm inclusions and estimate their size and proportion in a PGE budget of Cr-spinel. Furthermore, the calculation of this budget (see below) shows that the contribution of the inclusions detected by LA ICP-MS is small (~ 5% for Pt) compared to that of PGM found by SEM. Thus, although the LA ICP-MS – based estimations should be treated as semiquantitative, they are useful for the purpose of this study.

Calculation of PGE budget in Cr-spinel

Total content of PGE in “bulk Cr-spinel” was calculated as a sum of average PGE admixture and content of PGE stored as PGM inclusions. Average PGE admixtures are their median with an uncertainty taken as 1 standard deviation values (Table S8). Content of Pt stored as Pt-Fe alloy inclusions was calculated as a sum of those estimated from SEM data (487 ppb) and estimated from LA ICP-MS analyses (23 ppb) (Eq. 7) (Tables S4, S6). Because of a multitude of factors in a calculation and unparametrized errors of many of them, it was impossible to calculate an error of the LA ICP-MS estimation and, in addition, it would not affect the result too much due to the low (5%) proportion of the LA ICP-MS data contribution. Thus, the error for the resulting Pt-in-Cr-spinel value has been taken as that calculated for the SEM-based estimation: +23% and – 29% (Fig. 10A). Contents of Os, Ir and Rh, stored as PGM inclusions in Cr-spinel, have been calculated as a sum of those estimated from LA ICP-MS analyses and those which are present in Pt-Fe alloys found by SEM (taken as an average admixture in Pt-Fe alloys according to EDS data) (Tables S5, S6, S8). Similarly, the relative errors for Os, Ir and Rh values accommodated as in Cr-spinel hosted inclusions have been taken as + 23% and – 29% of their average contents in Pt-Fe alloys. The results of these calculations can be found in Table S8.

Calculation of olivine + Cr-spinel accumulation trends

Model trends envisaging behavior of Rh, Ir and Pt along the Ol – Cr-spinel cotectic have been calculated based on the following assumptions.

1. Picrites are mixtures of a primitive melt (carrying melt) and accumulated olivine and Cr-spinel crystals (cumulate). Contents of PGE in the carrying melt are equal to their estimated contents in the primitive melt.
2. Gross PGE content in Cr-spinel corresponds to the sum of PGE stored as admixture and PGM inclusions.
3. Since PGM concentrations in olivine turn out to be below detection limits of LA ICP MS, values corresponding to these detection limits can be taken as maximal PGE contents in olivine.

Note that under this assumption the modelled mixture (melt + crystals) contains the highest possible amount of PGE because the primitive melt is richer in Rh, Ir and Pt than the fractionated melt (Fig. 2B-D). Cr-spinel to olivine cotectic proportion has been set 1.3 : 98.7 as follows from the MgO-Cr regression (Fig. 2A). The average trends (dashed red lines on Fig. 2B-D) denote model Cr and PGE contents in mixtures of Cr-spinel, olivine and primitive melt if (1) PGE contents accommodated by Cr-spinel are equal to their average (admixture + PGM inclusions) calculated values, (2) PGE contents in olivine are negligible (Table S8). The pink fields around these lines cover the uncertainty ranges laying between minimal and maximal estimations of total PGE contents in Cr-spinel (according to the errors calculated for those contents – see previous paragraph) (Table S8). The grey dashed lines (Fig. 1C, D) denote “extreme” cases of the highest possible Ir and Pt accumulation if (1) PGE contents in Cr-spinel are equal to their highest (admixture + PGM inclusions) calculated values, (2) PGE contents in olivine are equal to the LA ICP MS detection limits (1 ppb for Ir and 3 ppb for Pt) (Table S8).

Data availability

The geochemical data underlying this manuscript is stored in the EarchChem Library (ECL) and are available at <https://doi.org/10.60520/IEDA/11357862>. Other data, including supplementary datasets and supplementary figures, have been deposited in Zenodo and are available at <https://doi.org/10.5281/zenodo.14196687>. The script used for the statistical modelling of inclusions size distribution is available on https://github.com/SergeyEKonsantinov/RelArea_estimator.git.

Received: 18 December 2024; Accepted: 3 April 2025

Published online: 24 April 2025

References

1. Barnes, S. J., Holwell, D. A. & Le Vaillant, M. Magmatic sulfide ore deposits. *Elements* **13**, 89–95 (2017).
2. Naldrett, A. J. In *Magmatic Sulfide Deposits: Geology, Geochemistry and Exploration*. 481–612. (Springer, 2004).
3. Holwell, B. D. & McDonald, I. A review of the behaviour of platinum group elements within natural magmatic sulfide ore systems. *Platin. Met. Rev.* **54**, 26–36 (2010).
4. Augé, T., Genna, A., Legendre, O., Ivanov, K. S. & Volchenko, Y. A. Primary platinum mineralization in the Nizhny Tagil and Kachkanar ultramafic complexes, Urals, Russia: A genetic model for PGE concentration in chromite-rich zones. *Econ. Geol.* **100**, 707–732 (2005).
5. Finnigan, C. S., Brenan, J. M., Mungall, J. E. & McDonough, W. Experiments and models bearing on the role of chromite as a collector of platinum group minerals by local reduction. *J. Pet.* **49**, 1647–1665 (2008).
6. Hiemstra, S. The role of collectors in the formation of the platinum deposits in the bushveld complex. *Can. Mineral.* **17**, 469–482 (1979).
7. Barnes, S. J. & Ripley, E. M. Highly siderophile and strongly chalcophile elements in magmatic ore deposits. *Rev. Mineral. Geochem.* **81**, 725–774 (2016).
8. Prichard, H. M., Barnes, S. J., Fisher, P. C., Pagé, P. & Zientek, M. L. Laurite and associated PGM in the Stillwater chromitites: implications for processes of formation, and comparisons with laurite in the bushveld and ophiolitic chromitites. *Can. Mineral.* **55**, 121–144 (2017).
9. Mina, A. & Anenburg, M. Finding and identifying platinum group elements in the Eastman layered mafic intrusion. *Aust. J. Earth Sci.* **71**, 1170–1182. <https://doi.org/10.1080/08120099.2024.2375063> (2024).

10. Arguin, J. P., Pagé, P., Barnes, S. J., Yu, S. Y. & Song, X. Y. The effect of chromite crystallization on the distribution of osmium, Iridium, ruthenium and rhodium in picritic magmas: an example from the Emeishan large igneous Province, Southwestern China. *J. Petrol.* **57**, 1019–1048 (2016).
11. Greenough, J. D. & Fryer, B. J. Behavior of the platinum-group elements during differentiation of the North mountain basalt, Nova Scotia. *Can. Mineral.* **33**, 153–163 (1995).
12. Ireland, T. J., Walker, R. J. & Garcia, M. O. Highly siderophile element and 187Os isotope systematics of Hawaiian Picrites: implications for parental melt composition and source heterogeneity. *Chem. Geol.* **260**, 112–128 (2009).
13. Kutuyev, A. V. et al. Primitive high-K intraoceanic Arc magmas of Eastern Kamchatka: implications for Paleo-Pacific tectonics and magmatism in the cretaceous. *Earth Sci. Rev.* **220**, 103703 (2021).
14. Park, J. W., Campbell, I. H. & Arculus, R. J. Platinum-alloy and sulfur saturation in an arc-related basalt to rhyolite suite: evidence from the pual ridge lavas, the Eastern Manus basin. *Geochim. Cosmochim. Acta.* **101**, 76–95 (2013).
15. Park, J. W., Campbell, I. H., Kim, J. & Moon, J. W. The role of late sulfide saturation in the formation of a Cu- and Au-rich Magma: insights from the platinum group element geochemistry of Niutahi–Motutahi lavas, Tonga Rear Arc. *J. Pet.* **56**, 59–81 (2015).
16. Pitcher, L., Helz, R. T., Walker, R. J. & Piccoli, P. Fractionation of the platinum-group Elements and re during crystallization of basalt in Kilauea Iki lava lake, Hawaii. *Chem. Geol.* **260**, 196–210 (2009).
17. Barnes, S. J. Platinum-group element and trace element contents of chromite grains from the Alexo komatiite flows compared with chromites from other volcanic rocks: implications for the use of chromite compositions in petrogenesis. *Can. J. Mineralogy Petrol.* **62**, 659–681 (2024).
18. Brenan, J. M., Finnigan, C. F., McDonough, W. F. & Homolova, V. Experimental constraints on the partitioning of Ru, Rh, Ir, Pt and Pd between chromite and silicate melt: the importance of ferric iron. *Chem. Geol.* **302**, 16–32 (2012).
19. Capobianco, C. J. & Drake, M. J. Partitioning of ruthenium, rhodium, and palladium between spinel and silicate melt and implications for platinum group element fractionation trends. *Geochim. Cosmochim. Acta.* **54**, 869–874 (1990).
20. Pagé, P. & Barnes, S. J. The influence of chromite on osmium, Iridium, ruthenium and rhodium distribution during early magmatic processes. *Chem. Geol.* **420**, 51–68 (2016).
21. Pagé, P., Barnes, S. J., Bédard, J. H. & Zientek, M. L. In situ determination of Os, Ir, and Ru in chromites formed from komatiite, tholeiite and boninite magmas: implications for chromite control of Os, Ir and Ru during partial melting and crystal fractionation. *Chem. Geol.* **302**, 3–15 (2012).
22. Park, J. W., Campbell, I. H. & Eggins, S. M. Enrichment of Rh, Ru, Ir and Os in Cr spinels from oxidized magmas: evidence from the ambae volcano, Vanuatu. *Geochim. Cosmochim. Acta.* **78**, 28–50 (2012).
23. Park, J. W. et al. Empirical constraints on partitioning of platinum group elements between Cr-spinel and primitive terrestrial magmas. *Geochim. Cosmochim. Acta.* **216**, 393–416 (2017).
24. Fiorentini, M., Stone, W., Beresford, S. & Barley, M. Platinum-group element alloy inclusions in chromites from Archaean mafic-ultramafic units: evidence from the abitibi and the Agnew-Wiluna greenstone belts. *Mineral. Petrol.* **82**, 341–355 (2004).
25. Kamenetsky, V. S. et al. Crystallization of platinum-group minerals from silicate melts: evidence from Cr-spinel-hosted inclusions in volcanic rocks. *Geology* **43**, 903–906 (2015).
26. Locmelis, M., Pearson, N. J., Barnes, S. J. & Fiorentini, M. L. Ruthenium in komatiitic chromite. *Geochim. Cosmochim. Acta.* **75**, 3645–3661 (2011).
27. Ballhaus, C., Bockrath, C., Wohlgemuth-Ueberwasser, C., Laurenz, V. & Berndt, J. Fractionation of the noble metals by physical processes. *Contrib. Miner. Petrol.* **152**, 667–684 (2006).
28. Anenburg, M. & Mavrogenes, J. A. Experimental observations on noble metal nanonuggets and Fe-Ti oxides, and the transport of platinum group elements in silicate melts. *Geochim. Cosmochim. Acta.* **192**, 258–278 (2016).
29. Chayka, I. F. et al. Volcano–plutonic complex of the Tumrok range (Eastern Kamchatka): an example of the Ural-Alaskan type intrusion and related volcanic series. *Minerals* **13**, 126 (2023).
30. Kamenetsky, V. S., Sobolev, A. V., Joron, J. L. & Semet, M. P. Petrology and geochemistry of cretaceous ultramafic volcanics from Eastern Kamchatka. *J. Pet.* **36**, 637–662. <https://doi.org/10.1093/petrology/36.3.637> (1995).
31. Zinkevich, V., Danyushevskii, L. & Kamenetsky, V. Geology and petrochemistry of volcanogenic rocks of the Tumrok salient, Eastern Kamchatka. *Tikhookean Geol.* **5**, 84–98 (1991).
32. Konstantinovskaya, E. in *In Arc-Continent Collision*. (eds Brown, D., Paul, D. & Ryan) 247–277. (Springer, 2011).
33. Erlikh, E., Shantser, A. & Kutuyev, F. S. Meimechites of Eastern Kamchatka. *Izv. Akad. Nauk. SSSR Ser. Geol.* **3**–9. (1971).
34. Kamenetskiy, V., Portnyagin, M., Sobolev, A. & Danyushevskiy, L. Magna composition and crystallization conditions of the Picrite-Basalt suite in the Tumrok ridge, East Kamchatka. *Geochem. Int. C/c Geokhimiia.* **30**, 58–58 (1993).
35. Delesse, A. Procédé mécanique pour déterminer la composition des roches. *Ann. Min.* **13**, 379–388 (1848).
36. Weibel, E. R., Kistler, G. S. & Scherle, W. F. Practical Stereological methods for morphometric cytology. *J. Cell Biol.* **30**, 23–38 (1966).
37. Yudovskaya, M. A. et al. Behavior of highly-siderophile elements during magma degassing: A case study at the kudryavy volcano. *Chem. Geol.* **248**, 318–341 (2008).
38. Matveev, S. & Ballhaus, C. Role of water in the origin of podiform chromitite deposits. *Earth Planet. Sci. Lett.* **203**, 235–243 (2002).
39. Schoneveld, L. et al. Oxide-sulfide-melt-bubble interactions in spinel-rich taxitic rocks of the Norilsk-Talnakh intrusions, Polar Siberia. *Econ. Geol.* **115**, 1305–1320 (2020).
40. Borisov, A. Crystallization and stability of noble metal alloys in the magmatic process. *Geol. Ore Depos.* **47**, 469 (2005).
41. Borisov, A. & Palme, H. Solubilities of noble metals in Fe-containing silicate melts as derived from experiments in Fe-free systems. *Am. Mineral.* **85**, 1665–1673 (2000).
42. Brenan, J. M. & Andrews, D. High-temperature stability of laurite and Ru–Os–Ir alloy and their role in PGE fractionation in mafic magmas. *Can. Mineral.* **39**, 341–360 (2001).
43. Mungall, J. In *9th Internat. Platinum Symp., abstract with programs; Billings, Montana.* 321–324.
44. González-Jiménez, J. M. & Reich, M. An overview of the platinum-group element nanoparticles in mantle-hosted chromite deposits. *Ore Geol. Rev.* **81**, 1236–1248 (2017).
45. Evans, K. et al. The origin of platinum group minerals in oceanic crust. *Geology* **51**, 554–558 (2023).
46. Tenuta, S. et al. Nanoscale Os isotopic quantification of Wadi Tayin Dunite platinum group minerals by atom probe tomography. *Lithos* **488**, 107841 (2024).
47. Savard, D., Barnes, S. J. & Meisel, T. Comparison between nickel-sulfur fire assay Te co-precipitation and isotope Dilution with high-pressure Asher acid digestion for the determination of platinum-group elements, rhenium and gold. *Geostand. Geoanal. Res.* **34**, 281–291 (2010).
48. Cabri, L. J. (ed) *The Geology, Geochemistry, Mineralogy and Mineral Beneficiation of Platinum-Group Elements*. Canadian Institute of Mining, Metallurgy and Petroleum. (2002).
49. Cabri, L. J., Kelvin, M., Yang, Z., Jackson, S. E. & Altun, O. Application of LA-ICP-MS trace-element analysis for precious metal deportment: a case study of the Kevitsa mine, Finland. *Eur. J. Mineral.* **29**, 635–644 (2017).
50. Mansur, E. T., Barnes, S. J. & Duran, C. J. An overview of chalcophile element contents of pyrrhotite, Pentlandite, chalcopyrite, and pyrite from magmatic Ni-Cu-PGE sulfide deposits. *Miner. Depos.* **56**, 179–204 (2021).
51. Mansur, E. T., Barnes, S. J., Duran, C. J. & Sluzhenikin, S. F. Distribution of chalcophile and platinum-group elements among pyrrhotite, Pentlandite, chalcopyrite and Cubanite from the Norilsk-Talnakh ores: implications for the formation of platinum-group minerals. *Miner. Depos.* **55**, 1215–1232 (2020).

52. O'Driscoll, B. & González-Jiménez, J. M. Petrogenesis of the platinum-group minerals. *Rev. Miner. Geochem.* **81**, 489–578 (2016).
53. Godel, B., Barnes, S. J., Barnes, S. J. & Maier, W. D. Platinum ore in three dimensions: insights from high-resolution X-ray computed tomography. *Geology* **38**, 1127–1130 (2010).
54. Barnes, S. J. et al. Spatial association between platinum minerals and magmatic sulfides imaged with the Maia mapper and implications for the origin of the chromite-sulfide-PGE association. *Can. Mineral.* **59**, 1775–1799 (2021).
55. Godel, B. & Barnes, S. J. Platinum-group elements in sulfide minerals and the whole rocks of the JM reef (Stillwater Complex): Implication for the formation of the reef. *Chem. Geol.* **248**, 272–294 (2008).
56. Norris, A. & Danyushevsky, L. Towards estimating the complete uncertainty budget of quantified results measured by LA-ICP-MS. *Goldschmidt.* (2018).
57. Longerich, H. P., Jackson, S. E. & Günther, D. Inter-laboratory note. Laser ablation inductively coupled plasma mass spectrometric transient signal data acquisition and analyte concentration calculation. *J. Anal. At. Spectrom.* **11**, 899–904 (1996).
58. Hrstka, T., Gottlieb, P., Skala, R., Breiter, K. & Motl, D. Automated mineralogy and petrology-applications of TESCAN integrated mineral analyzer (TIMA). *J. Geosci.* **63**, 47–63 (2018).
59. Hull, F. & Houk, W. Statistical grain structure studies: plane distribution curves of regular polyhedrons. *JOM* **5**, 565–572 (1953).
60. Halter, W. E., Pettke, T., Heinrich, C. A. & Rothen-Rutishauser, B. Major to trace element analysis of melt inclusions by laser-ablation ICP-MS: methods of quantification. *Chem. Geol.* **183**, 63–86 (2002).
61. Karasev, A. V. & Suito, H. Measurement of inclusion size by laser ablation ICP mass spectrometry. *ISIJ Int.* **44**, 356–363 (2004).
62. Chayka, I. F. et al. Major, trace, and platinum-group elements in the Late Cretaceous arc volcano-plutonic complex of the Tumrok Range, eastern Kamchatka. Interdisciplinary Earth Data Alliance (IEDA). <https://doi.org/10.60520/IEDA/113578>. (Accessed 4 Feb 2025).
63. Shapiro, M. & Solov'ev, A. Formation of the Olyutorsky–Kamchatka foldbelt: A kinematic model. *Russ. Geol. Geophys.* **50**, 668–681 (2009).
64. Lyubetskaya, T. & Korenaga, J. Chemical composition of Earth's primitive mantle and its variance: 1. Method and results. *J. Geophys. Res. Solid Earth* **112** (2007).
65. Righter, K., Campbell, A., Humayun, M. & Hervig, R. Partitioning of Ru, Rh, Pd, re, Ir, and Au between Cr-bearing Spinel, Olivine, pyroxene and silicate melts. *Geochim. Cosmochim. Acta.* **68**, 867–880 (2004).

Acknowledgements

We dedicate this study to hallowed memory of our dear colleague Dmitry Varlamov, who assisted with SEM, and has unexpectedly passed away in November 2024. The authors thank Maya Kamenetsky, Karsten Goemann, Vasilii Belyaev, Michael Khlestov, Nikolay Karmanov, Dany Savard, Audrie Lavoie and Viktoria Danilovskaya for the analytical works; Anton Nuzhdaev and Dmitry Saveliev – for the help in field works; Michael Zelensky – for an informal discussion. We thank Michael Anenburg for his thoughtful review and editor Xingcheng Liu for managing the editorial process. Vadim S. Kamenetsky in the Insititue of Oceanology, CAS, was funded by the National Natural Science Foundation of China No. W2431032. This study is a part of the research topic of the Institute of Experimental Mineralogy, Russian Academy of Sciences, project no. FMUF-2022-0004. This study was partially supported by the research topic of the IVS FEB RAS "Mineral formation in the supra-subduction zone of the North Pacific" (No. FWME-2024-0004). This study was partially supported by the DSTI-NRF Centre of Excellence (CoE) for Integrated Mineral and Energy Resource Analysis (DSTI-NRF CIMERA). Opinions expressed and conclusions arrived at, are those of the authors and are not necessarily to be attributed to the CoE. SEM investigations were partially supported by Russian Science Foundation (project number 24-77-00099). Field works and sample preparation were supported by Russian Science Foundation (project number 21-17-00122). Laser ablation ICP-MS analyses in China University of Geosciences (Wuhan) were supported by National Natural Science Foundation of China No. 42073036. Statistical modelling is done in Novosibirsk State University and partially supported by the Ministry of Science and Higher Education of the Russian Federation (project № FSUS-2020-0039).

Author contributions

I. F. C.: Conceptualization, Investigation, Writing – original draft, Visualisation, Data curation, Methodology, Funding acquisition, Supervision. V. S. K.: Conceptualization, Investigation, Writing – original draft, Funding acquisition, Supervision. A. V. K.: Conceptualization, Writing – original draft, Investigation. S.-J. B.: Investigation, Writing – review and editing. A. S. S.: Methodology, Investigation, Data curation, Writing – review and editing, Funding acquisition. S. E. K.: Methodology, Data curation, Writing – original draft. N. I. B.: Investigation, Data curation, Visualization. S. G. K.: Methodology, Investigation. I. A. B.: Investigation. I. A. Z.: Investigation. V. D. S.: Investigation. V. M. K.: Investigation. A. V. I.: Investigation. N. V. B.: Investigation. J.-W. P.: Writing – review and editing.

Declarations

Competing interests

The authors declare no competing interests.

Additional information

Supplementary Information The online version contains supplementary material available at <https://doi.org/10.1038/s41598-025-97281-z>.

Correspondence and requests for materials should be addressed to V.S.K.

Reprints and permissions information is available at www.nature.com/reprints.

Publisher's note Springer Nature remains neutral with regard to jurisdictional claims in published maps and institutional affiliations.

Open Access This article is licensed under a Creative Commons Attribution-NonCommercial-NoDerivatives 4.0 International License, which permits any non-commercial use, sharing, distribution and reproduction in any medium or format, as long as you give appropriate credit to the original author(s) and the source, provide a link to the Creative Commons licence, and indicate if you modified the licensed material. You do not have permission under this licence to share adapted material derived from this article or parts of it. The images or other third party material in this article are included in the article's Creative Commons licence, unless indicated otherwise in a credit line to the material. If material is not included in the article's Creative Commons licence and your intended use is not permitted by statutory regulation or exceeds the permitted use, you will need to obtain permission directly from the copyright holder. To view a copy of this licence, visit <http://creativecommons.org/licenses/by-nc-nd/4.0/>.

© The Author(s) 2025